CLIP Meets Diffusion: A Synergistic Approach to Anomaly Detection

Anonymous authors
Paper under double-blind review

Abstract

Anomaly detection is a complex problem due to the ambiguity in defining anomalies, the diversity of anomaly types (e.g., local and global defect), and the scarcity of training data. As such, it necessitates a comprehensive model capable of capturing both low-level and high-level features, even with limited data. To address this, we propose CLIPFUSION, a method that leverages both discriminative and generative foundation models. Given the CLIP-based discriminative model's limited capacity to capture fine-grained local details, we incorporate a diffusion-based generative model to complement its features. This integration yields a synergistic solution for anomaly detection. To this end, we propose using diffusion models as feature extractors for anomaly detection, and introduce carefully designed strategies to extract informative cross-attention and feature maps. Experimental results on benchmark datasets (MVTec-AD, VisA) demonstrate that CLIPFUSION consistently outperforms baseline methods in both anomaly segmentation and classification under both zero-shot and few-shot settings. We believe that our method underscores the effectiveness of multi-modal and multi-model fusion in tackling the multifaceted challenges of anomaly detection, providing a scalable solution for real-world applications.

1 Introduction

Anomaly detection is an important problem in real-world applications such as industry (Bergmann et al., 2019; Zou et al., 2022) and medicine (Setio et al., 2017; Menze et al., 2014). In this paper, we address anomaly classification and segmentation.[1] In anomaly classification (or segmentation), each image (or pixel) is classified as normal or anomalous.

In practice, the number of abnormal images is small, while the potential types of abnormalities are highly diverse, making it challenging to obtain representative examples. Moreover, developing methods that can quickly adapt to new environments (e.g., new processes or products), even with a limited number of normal images, has become a critical research topic (Rudolph et al., 2021; Sheynin et al., 2021; Zou et al., 2022; Huang et al., 2022). To address this, we focus on the problem within the zero-shot or few-normal-shot[2] setup.

The recent advent of large-scale pretrained foundation models, e.g., GPT (Brown et al., 2020) and DALL-E (Ramesh et al., 2021; 2022), has opened new horizons for addressing such challenges. The generalizability and scalability of foundation models make them particularly effective for tackling zero-shot and few-shot tasks such as anomaly detection. In this paper, we present a novel methodology that combines the complementary strengths of discriminative and generative foundation models.

Anomaly detection is a multifaceted problem, and various approaches have been developed based on different perspectives. First, anomaly detection has the aspect of one-class classification. This has led the community to methods that learn normality from normal images and judge what deviates from it as anomalous. Here,

[1] It is also referred to as anomaly detection and localization, respectively, in the literature. We use the terms anomaly classification and segmentation, and refer to anomaly detection as the overarching problem encompassing both.

[2] In this paper, "few-shot" specifically refers to "few-normal-shot".

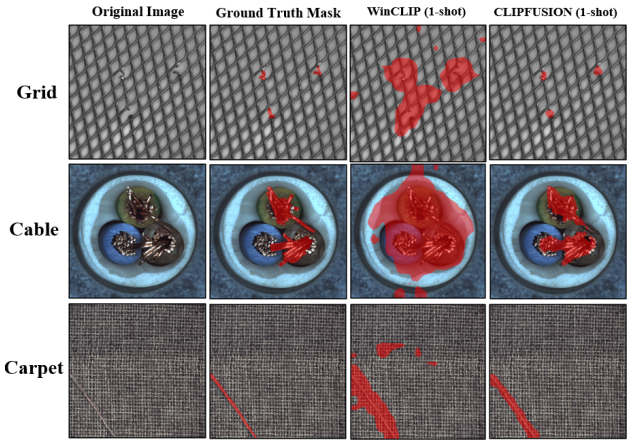

Figure 1: Qualitative results of our model CLIPFUSION. It captures fine-grained anomalies more effectively than WinCLIP.

many methods extract normal features from normal images using a vision foundation model (Cohen & Hoshen, 2020; Defard et al., 2021; Roth et al., 2022). Second, anomaly detection has the aspect of two-class classification. The community has employed vision-language foundation models, such as CLIP (Radford et al., 2021), to compare a query image against normal and abnormal text prompts (Jeong et al., 2023; Li et al., 2024a). Third, anomaly detection also has the aspect of semantic segmentation. Many anomalous features are fine-grained ones that appear in textures or edges. WinCLIP (window-based CLIP) attempted to solve this by sliding windows at multiple scales. However, it is known that CLIP has limitations in learning fine-grained features (Wysoczańska et al., 2025; Jiang et al., 2023), and such an approach might be suboptimal. Also, it requires hundreds of forward passes due to the exhaustive sliding of multi-scale windows.

The multifaceted nature of anomaly detection makes it challenging to address using only discriminative models. So, we aim to create synergy by fusing a discriminative vision-language model (VLM) with a generative text-to-image (T2I) model. These are two fundamentally distinct approaches to aligning images and text. Discriminative models, such as CLIP, directly align embeddings in the same space, while generative models, like diffusion models, align them indirectly by jointly performing a common task. Diffusion models align images and text through a generative process that preserves fine-grained semantics. Consequently, they may capture more detailed visual patterns. Therefore, it can be beneficial to leverage both high-level information extracted from the CLIP-based model and low-level information extracted from the diffusion-based model for effective anomaly detection.

We propose CLIPFUSION (= CLIP + Diffusion), a novel method that combines the strengths of multi-modal (language and vision) and multi-model (CLIP and diffusion) approaches. In the zero-shot scenario, CLIPFUSION effectively identifies anomalies by integrating image-text alignment from a CLIP-based model and cross-attention maps (Chefer et al., 2023; Zhang et al., 2023b; Liu et al., 2024) from a diffusion-based model. In the few-shot scenario, it further enhances its performance by additionally leveraging feature maps from the CLIP image encoder and the diffusion denoiser, enabling a more comprehensive comparison between the query image and reference images. Figure 1 illustrates qualitative results, showcasing the model's ability to capture fine-grained anomalies. CLIPFUSION exemplifies a holistic framework that synergizes complementary foundation models, and has the potential to extend beyond anomaly detection and advance other recognition tasks.

Contributions of our work are summarized as follows:

- We propose the use of diffusion models as feature extractors for anomaly detection. To this end, we exploit cross-attention and feature maps and carefully design extraction strategies. Since we

extract intermediate features from an off-the-shelf diffusion model without any training or iterative denoising, our method is fast and efficient.

- We introduce a novel approach to anomaly detection that jointly leverages features from CLIP and diffusion models. We demonstrate the complementary benefits of combining features from both models. Since diffusion models compensate for CLIP's limitations in capturing fine-grained local details, our method eliminates the need for time-consuming techniques such as multi-scale sliding windows.

- In terms of performance, our method consistently outperforms baselines. Unlike most prior works, it is also versatile in scope: it can handle both segmentation and classification tasks under zero-shot and few-shot settings.

- Our method requires no additional training, which enables fast real-world deployment. Even in few-shot settings, the samples are used solely for feature extraction rather than training, making the method more robust. In contrast, training-based methods are sensitive to the choice of when to stop training, which is challenging in few-shot setups due to the absence of a validation set.

2 Related Work

Vision(-Language) Models for Anomaly Detection In works that utilize vision(-language) models in anomaly detection, features are extracted from the intermediate layers of a model pretrained on a discriminative task (e.g., classification or contrastive learning). Anomaly detection is performed by comparing the features of the query image with the features of reference images. Some works utilize ResNet-based models pretrained on ImageNet in the few-shot regime. In SPADE (Cohen & Hoshen, 2020), a k-nearest neighbors algorithm is employed to identify the k reference images closest to the query image, which are then used as the basis for anomaly detection. In PaDiM (Defard et al., 2021), features extracted from reference images are modeled as Gaussian distributions, and the features of the query image are compared against these distributions. In PatchCore (Roth et al., 2022), a memory bank is constructed using the features of reference images, and the features of a query image are directly compared against this memory bank. WinCLIP (Jeong et al., 2023) applies local windows and combines the results through harmonic aggregation. PromptAD (Li et al., 2024a) learns prompt tokens through contrastive training.

A separate line of work assumes access to additional data and leverages it. Some methods require an auxiliary dataset containing both normal and anomaly images, e.g., training on the MVTec-AD dataset and inference on the VisA dataset (Hu et al., 2024; Zhu & Pang, 2024; Yao et al., 2024; Li et al., 2024c; Cao et al., 2024; Zhou et al., 2023; Gu et al., 2024a; Qu et al., 2024). AnomalyGPT (Gu et al., 2024b) relies on an auxiliary dataset with a large number of normal samples. In practice, acquiring such data with matching characteristics is challenging, and these methods often struggle when deployed on datasets with distribution shifts. Moreover, the need for additional training increases deployment time. Some methods also rely on ground-truth segmentation masks, which are difficult to obtain in real-world scenarios (Hu et al., 2024; Cao et al., 2024; Zhou et al., 2023). MuSc (Li et al., 2024b) leverages the test set by exhaustively comparing the features of all test images, which is only feasible when the entire test set is available and contains a low proportion of anomalies.

Diffusion Models for Discriminative Tasks Recently, there has been growing interest in applying diffusion models to discriminative tasks (Fuest et al., 2024). In DDPM-Seg (Baranchuk et al., 2021), feature maps are constructed using activations extracted from intermediate layers of the denoiser and are utilized for semantic segmentation. VPD (Zhao et al., 2023) further incorporates cross-attention maps for semantic segmentation and depth estimation. These methods require fine-tuning for downstream tasks. On the other hand, DiffusionClassifier (Li et al., 2023a) performs zero-shot classification by determining which text conditioning best predicts the noise. P2PCAC (Hertz et al., 2022) and USCSD (Hedlin et al., 2024) reveal that cross-attention maps contain rich information about spatial layouts through image editing and semantic correspondence tasks.

3 Preliminaries

CLIP CLIP (Radford et al., 2021) consists of an image encoder $f_I(x)$ and a text encoder $f_T(c)$. These encoders map images and texts into the same embedding space. The model is trained to match correct image-text pairs with high similarity while assigning low similarity to incorrect pairs. This process is optimized using the following contrastive loss (Chen et al., 2020):

$$p(T = \hat{c}|I = x) := \frac{\exp(\text{sim}(f_I(x), f_T(\hat{c}))/\tau)}{\sum_{c\in\mathcal{C}} \exp(\text{sim}(f_I(x), f_T(c))/\tau)}, \tag{1}$$

where $\mathcal{C}$ is the set of candidate text prompts, $\tau > 0$ is the temperature hyperparameter, and $\text{sim}(\cdot, \cdot)$ is the cosine similarity measure.

Diffusion A diffusion model (Ho et al., 2020) is trained through a sequential process that involves forward diffusion and backward denoising. In the diffusion process, random noise is progressively added to a clean image over several steps, following the equation:

$$q(x_t|x_{t-1}) = \mathcal{N}(x_t; \sqrt{1-\beta_t}\, x_{t-1}, \beta_t\, \mathbf{I}), \tag{2}$$

where β_t is the noise schedule hyperparameter, which determines the amount of noise added to the image x_{t-1} (Nichol & Dhariwal, 2021). In the denoising process, random noise is progressively removed over several steps using the following equation to restore the original image:

$$p_\theta(x_{t-1}|x_t) = \mathcal{N}(x_{t-1}; \mu_\theta(x_t, t), \Sigma_\theta(x_t, t)). \tag{3}$$

In this process, the denoiser $\epsilon_\theta(x_t, t)$ learns to predict the added noise from the noisy image x_t at a given time step t (Song et al., 2020). During inference, random noise is sampled, and the denoiser iteratively removes it to generate a new image. By conditioning on a text prompt c, the denoiser $\epsilon_\theta(x_t, t, c)$ guides the generation process to align the resulting image with the provided text. Diffusion models demonstrate superior performance in understanding image details by generating high-quality images compared to other generative models (Dhariwal & Nichol, 2021). They can also be utilized for inpainting a specific region of an image. At each step, the untouched region is preserved by replacing it with the corresponding part of the original image, ensuring that only the specified region is generated and seamlessly blended with the rest of the image (Rombach et al., 2021).

4 Method

The final model, CLIPFUSION, is a fusion of our CLIP-based and diffusion-based models. For convenience, we call the CLIP-based model PatchCLIP (patch-based CLIP) and the diffusion-based model MapDiff (map-based diffusion). We first outline our feature extraction strategies from both models, tailored for anomaly detection.

PatchCLIP CLIP processes an image by dividing it into multiple patches and outputs both patch embeddings and a class token embedding. While the class token embedding is aligned with text embeddings, patch embeddings can provide additional information, which we incorporate to enrich the spatial representation. Given that fine-grained details are handled by the diffusion-based model, PatchCLIP provides a simple yet effective spatial prior, thereby avoiding the cumbersome multi-scale window sliding in WinCLIP.

Additionally, we utilize features extracted from CLIP's image encoder. To achieve this, we make use of the VV-attention mechanism proposed in CLIP surgery (Li et al., 2023b; 2024a). This mechanism was introduced to complement CLIP's QK-attention mechanism, which is specialized in global feature extraction. It facilitates local feature extraction by enabling direct interactions between values (hence the name VV-attention) that carry information about the patches themselves.

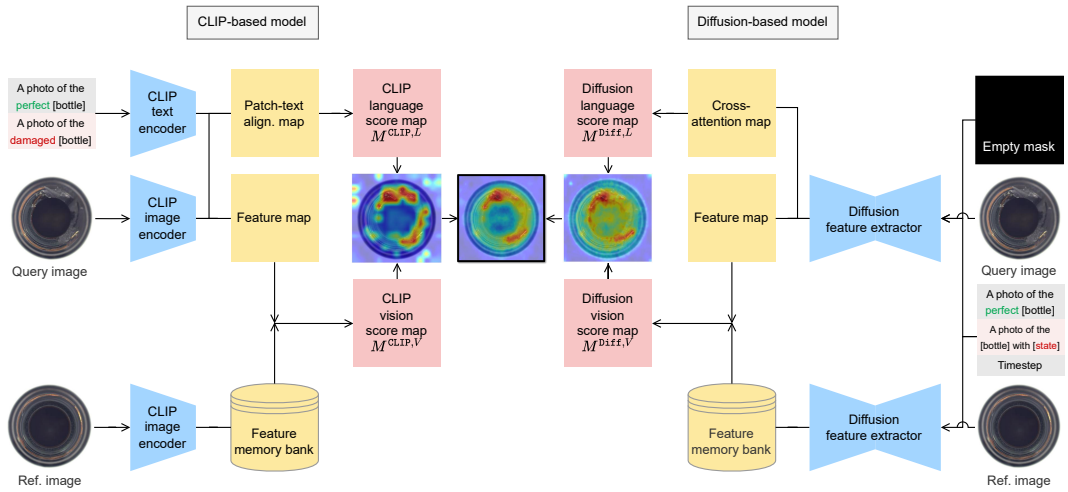

Figure 2: Overall framework for CLIPFUSION. The CLIP-based model and the diffusion-based model process query and reference images to generate anomaly maps. The final anomaly map is obtained by fusing the outputs of the vision and language components of both models.

MapDiff We extract and utilize cross-attention maps and feature maps from the diffusion denoiser. To achieve this, we use an inpainting pipeline that takes a clean image as input, rather than a generation pipeline that starts with random noise. In the inpainting pipeline, a mask is provided to specify the region where noise will be added. Here, we use the trick of applying an empty mask. This prevents noise from being added, but the denoiser still perceives the original image as noisy, thereby allowing us to control the timestep and extract features at the desired level of detail.

By passing the clean image through the denoiser once, we extract the maps from its intermediate layers. A large timestep makes the denoiser interpret the image as highly noisy, capturing high-level pattern information, while a small timestep emphasizes finer details.

4.1 Anomaly Segmentation

The final anomaly score map $M \in \mathbb{R}^{H \times W}$ for segmentation is obtained by fusing the score maps from PatchCLIP and MapDiff. In the zero-shot setup, only the language-guided score maps $M^{\texttt{CLIP},L}$ and $M^{\texttt{Diff},L}$ are used. In the few-shot setup, the vision-guided score maps $M^{\texttt{CLIP},V}$ and $M^{\texttt{Diff},V}$ are additionally incorporated. The final anomaly score map is computed as follows:

$$M := \alpha(M^{\texttt{CLIP},L} + M^{\texttt{CLIP},V}) + (1-\alpha)(M^{\texttt{Diff},L} + M^{\texttt{Diff},V}), \tag{4}$$

where α is the weight between the models. In the zero-shot setup, $M := \alpha M^{\texttt{CLIP},L} + (1-\alpha)M^{\texttt{Diff},L}$.

4.1.1 Zero-shot

In the zero-shot setup, given a query image, we leverage the relationships between images and texts learned by multi-modal models to create anomaly score maps.

CLIP Language-guided Score Map $M^{\texttt{CLIP},L}$ The query image is input to the CLIP image encoder (e.g., ViT), which divides it into patches, processes them, and outputs patch embeddings. On the other hand, normal and abnormal text prompts are passed to the CLIP text encoder, producing normal and abnormal text embeddings. Then, the degree (Equation 1) to which each patch embedding is aligned to the abnormal text embedding is calculated for all patches and organized into a map. This is upsampled to the original image size through interpolation to obtain $M^{\texttt{CLIP},L}$.

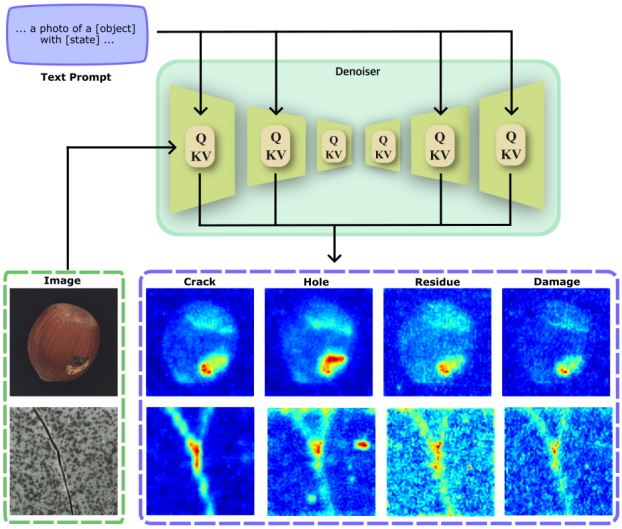

Figure 3: Examples of cross-attention maps extracted from a diffusion denoiser.

Diff Language-guided Score Map $M^{\texttt{Diff},L}$ The query image is passed to the diffusion inpainting pipeline along with an empty mask, a timestep, and a text prompt. The text prompt includes an object word and a state word, for example:

"`a photo of a [object] with [state].`"

where `[object]` refers to the entity (e.g., "`bottle`") in the image, and `[state]` describes a possible abnormal condition (e.g., "`crack`") of it. The `[state]` token interacts with the image as it passes through the denoiser (e.g., U-Net), generating a cross-attention map. The cross-attention map of a diffusion model is a heatmap showing where and how strongly a text token is attended to across image locations. Because we use a token that denotes an anomalous state, the attention weight at a location serves as a proxy for anomaly likelihood. That is, a higher value at a specific location in the map indicates that the location responds more strongly to the `[state]` token (i.e., the abnormal condition). Therefore, we can use this cross-attention map as an anomaly score map (Figure 3). Additionally, we calculate the average of cross-attention maps derived using various possible abnormal conditions (e.g., "`crack`", "`hole`", "`residue`", "`damage`") to obtain $M^{\texttt{Diff},L}$.

This can be interpreted as follows. In anomaly segmentation, given an image $I = x$, we are interested in the probability that the (h, w)-th pixel is abnormal ($A_{h,w} = 1$). This probability can be expressed as follows by conditioning on a text prompt $T = c$:

$$p(A_{h,w} = 1|I = x) = \sum_{c \in \mathcal{C}} p(A_{h,w} = 1|I = x, T = c)p(T = c), \tag{5}$$

where $\mathcal{C}$ represents the set of text prompts that describe abnormal conditions. Assuming that the text prompt T is uniform and interpreting $p(A_{h,w} = 1|I = x, T = c)$ as the cross-attention map intensity at the corresponding location:

$$M^{\texttt{Diff},L}_{h,w} := \frac{1}{|\mathcal{C}|} \sum_{c \in \mathcal{C}} p(A_{h,w} = 1|I = x, T = c). \tag{6}$$

4.1.2 Few-shot

In the few-shot setup, normal reference images are utilized. For the k-shot case, k images are used to construct feature memory banks, which are then compared with the features of the query image. In general, we extract normal features from normal reference images by passing them through the CLIP image encoder and the diffusion denoiser. Then, the query image is passed through and the extracted features are compared with the normal features. The degree of deviation is used as an anomaly score.

CLIP Vision-guided Score Map $M^{\texttt{CLIP},V}$ The reference images are passed through the CLIP's image encoder to extract reference features and stored in the memory bank. Features with low-level semantic information are extracted from a middle encoder block, while those with high-level semantic information come from a later encoder block.

The set of reference features extracted from the encoder block b is denoted as $\mathcal{R}^b$. For a given encoder block b, the feature map extracted from the query image is denoted as $F^b \in \mathbb{R}^{H \times W \times D_b}$. Then, $M^{\texttt{CLIP},V}_{h,w}$ is calculated by comparing the feature $F^b_{h,w}$ with the reference features $r \in \mathcal{R}^b$, as follows:

$$M^{\texttt{CLIP},V}_{h,w} := \frac{1}{|\mathcal{B}|} \sum_{b \in \mathcal{B}} \min_{r \in \mathcal{R}^b} \frac{1}{2} \left(1 - \text{sim}(F^b_{h,w}, r)\right), \tag{7}$$

where $\mathcal{B}$ is the set of blocks b. That is, a score is computed based on the similarity, and the smallest among all reference features in $\mathcal{R}^b$ is conservatively used as the anomaly score for b. The final anomaly score is the average over $\mathcal{B}$.

Diff Vision-guided Score Map $M^{\texttt{Diff},V}$ Reference images are passed through the diffusion denoiser to extract features, which are stored in the memory bank. The denoiser consists of three parts: an encoder (down-blocks), a bottleneck (mid-block), and a decoder (up-blocks). Information in the encoder is passed to the decoder via skip connections. The bottleneck is the most compressed stage, where much of the detailed information is lost, making it unsuitable for feature extraction. Therefore, we extract features from the decoder. Specifically, we focus on the middle and later decoder blocks, as they provide the most semantically rich features (Baranchuk et al., 2021; Zhao et al., 2023).

When timestep t is given, the set of reference features extracted from the decoder block b is denoted as $\mathcal{R}^{t,b}$. The feature map extracted from the query image at timestep t and decoder block b is denoted as $F^{t,b} \in \mathbb{R}^{H \times W \times D_b}$. Then, $M^{\texttt{Diff},V}_{h,w}$ is calculated as follows:

$$M^{\texttt{Diff},V}_{h,w} := \frac{1}{|\mathcal{T}|} \sum_{(t,b) \in \mathcal{T}} \min_{r \in \mathcal{R}^{t,b}} \frac{1}{2} \left(1 - \text{sim}(F^{t,b}_{h,w}, r)\right), \tag{8}$$

where $\mathcal{T}$ is the set of combinations (t, b).

4.2 Anomaly Classification

The final anomaly score $S \in \mathbb{R}$ for classification is obtained by fusing four scores:

$$S := \alpha(S^{\texttt{CLIP},L} + S^{\texttt{CLIP},V}) + (1 - \alpha)(S^{\texttt{Diff},L} + S^{\texttt{Diff},V}). \tag{9}$$

In the zero-shot setup, only the language-guided scores are used. Specifically, the CLIP language-guided score $S^{\texttt{CLIP},L}$ is defined as the degree (Equation 1) of alignment between the query image's class token embedding and the abnormal text embedding. The diffusion language-guided score $S^{\texttt{Diff},L}$ aggregates the diffusion language-guided score map $M^{\texttt{Diff},L}$ and is defined as follows:

$$S^{\texttt{Diff},L} := 1 - \text{median}(M^{\texttt{Diff},L}) / \max(M^{\texttt{Diff},L}). \tag{10}$$

This means that the score becomes larger when the degree of focus of the cross-attention map is high, that is, when the maximum is significantly greater than the median.

In the few-shot setup, we additionally aggregate the vision-guided score maps, defining the scores as follows in accordance with common practice (Jeong et al., 2023):

$$S^{\texttt{CLIP},V} := \max(M^{\texttt{CLIP},V}), \;\; S^{\texttt{Diff},V} := \max(M^{\texttt{Diff},V}). \tag{11}$$

Table 1: Quantitative results for anomaly segmentation.

Setup	Method	MVTec-AD		VisA	
		AUROC	AUPRO	AUROC	AUPRO
0-shot	Trans-MM (Chefer et al., 2021)	57.5±0.0	21.9±0.0	49.4±0.0	10.2±0.0
	MaskCLIP (Zhou et al., 2022)	63.7±0.0	40.5±0.0	60.9±0.0	27.3±0.0
	WinCLIP (Jeong et al., 2023)	85.1±0.0	64.6±0.0	79.6±0.0	56.8±0.0
	CLIPFUSION (ours)	**90.9±0.0**	**87.1±0.0**	**92.1±0.0**	**83.3±0.0**
1-shot	PaDiM (Defard et al., 2021)	89.3±0.9	73.3±2.0	89.9±0.8	64.3±2.4
	PatchCore (Roth et al., 2022)	92.0±1.0	79.7±2.0	95.4±0.6	80.5±2.5
	WinCLIP (Jeong et al., 2023)	95.2±0.5	87.1±1.2	96.4±0.4	85.1±2.1
	PromptAD (Li et al., 2024a)	94.9±0.8	87.7±1.5	95.7±0.9	84.0±1.2
	CLIPFUSION (ours)	**95.8±0.1**	**90.4±0.1**	**97.3±0.1**	**87.0±0.3**
2-shot	PaDiM (Defard et al., 2021)	91.3±0.7	78.2±1.8	92.0±0.7	70.1±2.6
	PatchCore (Roth et al., 2022)	93.3±0.6	82.3±1.3	96.1±0.5	82.6±2.3
	WinCLIP (Jeong et al., 2023)	96.0±0.3	88.4±0.9	96.8±0.3	86.2±1.4
	PromptAD (Li et al., 2024a)	95.0±0.7	88.3±1.0	96.3±0.9	84.8±0.8
	CLIPFUSION (ours)	**96.3±0.1**	**91.4±0.2**	**97.7±0.1**	**87.3±0.2**
4-shot	PaDiM (Defard et al., 2021)	92.6±0.7	81.3±1.9	93.2±0.5	72.6±1.9
	PatchCore (Roth et al., 2022)	94.3±0.5	84.3±1.6	96.8±0.3	84.9±1.4
	WinCLIP (Jeong et al., 2023)	96.2±0.3	89.0±0.8	97.2±0.2	87.6±0.9
	PromptAD (Li et al., 2024a)	95.5±0.6	89.0±0.6	96.3±0.8	85.1±0.9
	CLIPFUSION (ours)	**96.8±0.1**	**92.1±0.2**	**98.0±0.1**	**87.7±0.5**

5 Comparisons

Datasets We use the MVTec-AD (Bergmann et al., 2019) and VisA (Zou et al., 2022) datasets, which are mainly used as benchmark datasets in anomaly detection. Each dataset consists of several object categories, and each object category is divided into a training set containing only normal images and a test set containing a mixture of normal and abnormal images. Query images are from the test set, and reference images are sampled from the training set.

Baseline methods We compare against methods with the same setup, that is, methods that use only the provided zero-shot or few-shot normal images and do not rely on any additional supervision. This setup reflects a realistic and challenging scenario commonly encountered in practice.

Specifically, we compare our method, CLIPFUSION, with methods utilizing vision models (PaDiM, PatchCore) and those utilizing vision-language models (CLIP-AC, Trans-MM, MaskCLIP, WinCLIP, PromptAD[3]). Note that, among these methods, only CLIPFUSION and WinCLIP are fully capable of handling both segmentation and classification tasks in both zero-shot and few-shot scenarios.

Experimental details For PatchCLIP, we employ OpenCLIP (Ilharco et al., 2021; Cherti et al., 2023; Schuhmann et al., 2022), which has been pretrained on LAION-400M (Schuhmann et al., 2021), using a Vision Transformer (ViT) (Dosovitskiy, 2020) as its image encoder. For MapDiff, we utilize the pretrained Stable Diffusion v2 model (Rombach et al., 2022), where the denoiser is based on U-Net (Ronneberger et al., 2015).

We set $\alpha = 0.25$ in Equation 4 for segmentation and $\alpha = 0.75$ in Equation 9 for classification to reflect the different importance of the models in each task. We report the average performance and standard deviations over five runs with different seeds. Further details are in Appendix A.2.

[3]The authors of PromptAD use the test set as a validation set during training to record the best performance for each category separately and report the aggregated results. For a fair comparison, we treat the training epoch as a fixed hyperparameter across categories and report the best-performing checkpoint reproduced using the official codebase. See Appendix A.5 for more details.

Table 2: Quantitative results for anomaly classification.

Setup	Method	MVTec-AD		VisA	
		AUROC	AUPR	AUROC	AUPR
0-shot	CLIP-AC (Radford et al., 2021)	74.0±0.0	89.1±0.0	59.3±0.0	67.0±0.0
	WinCLIP (Jeong et al., 2023)	91.8±0.0	96.5±0.0	78.1±0.0	81.2±0.0
	CLIPFUSION (ours)	**93.6±0.0**	**97.0±0.0**	**79.5±0.0**	**83.6±0.0**
1-shot	PaDiM (Defard et al., 2021)	76.6±3.1	88.1±1.7	62.8±5.4	68.3±4.0
	PatchCore (Roth et al., 2022)	83.4±3.0	92.2±1.5	79.9±2.9	82.8±2.3
	WinCLIP (Jeong et al., 2023)	93.1±2.0	96.5±0.9	83.8±4.0	85.1±4.0
	PromptAD (Li et al., 2024a)	92.6±1.0	95.7±0.9	83.1±2.1	85.7±1.2
	CLIPFUSION (ours)	**95.4±0.8**	**97.8±0.4**	**86.5±0.1**	**88.4±0.2**
2-shot	PaDiM (Defard et al., 2021)	78.9±3.1	89.3±1.7	67.4±5.1	71.6±3.8
	PatchCore (Roth et al., 2022)	86.3±3.3	93.8±1.7	81.6±4.0	84.8±3.2
	WinCLIP (Jeong et al., 2023)	94.4±1.3	97.0±0.7	84.6±2.4	85.8±2.7
	PromptAD (Li et al., 2024a)	93.2±1.0	96.1±1.0	85.0±1.8	87.2±1.8
	CLIPFUSION (ours)	**96.3±0.3**	**98.2±0.2**	**87.1±0.5**	**88.8±0.5**
4-shot	PaDiM (Defard et al., 2021)	80.4±2.5	90.5±1.6	72.8±2.9	75.6±2.2
	PatchCore (Roth et al., 2022)	88.8±2.6	94.5±1.5	85.3±2.1	87.5±2.1
	WinCLIP (Jeong et al., 2023)	95.2±1.3	97.3±0.6	87.3±1.8	88.8±1.8
	PromptAD (Li et al., 2024a)	93.8±0.7	96.5±0.7	86.2±1.6	88.1±1.9
	CLIPFUSION (ours)	**96.9±0.2**	**98.6±0.1**	**88.1±0.2**	**89.7±0.1**

5.1 Anomaly Segmentation

Table 1 presents a comparison of our method's performance with baseline methods for anomaly segmentation. The results show that CLIPFUSION consistently outperforms the baseline methods across all setups, datasets, and metrics. Our method, in particular, demonstrates dramatic performance improvements in the zero-shot setup. This highlights the critical contribution of the diffusion-based model's cross-attention map to zero-shot anomaly segmentation. Additionally, the significant performance improvements in the few-shot setup demonstrate how the diffusion-based model complements the CLIP-based model.

5.2 Anomaly Classification

Table 2 shows the performance comparison between our method and baseline methods for anomaly classification. CLIPFUSION consistently outperforms all baseline methods. This indicates that the diffusion-based model enhances performance not only in the segmentation task but also in the classification task by reinforcing local information.

In both segmentation and classification tasks, the consistent performance improvements as the number of shots increase highlight the scalability of our method with minimal additional data. Furthermore, the smaller standard deviations observed in our results indicate the robustness of our approach. This robustness can be attributed to the integration of multiple models, which mitigates the variability.

6 Empirical Study

In this section, results are reported under the one-shot setup.

6.1 Ablation Study

Table 3 presents the comparative performance of different models. As expected, the diffusion-based model, which captures local features effectively, performs better in the segmentation task, while the CLIP-based model, which captures global features effectively, performs better in the classification task. The combination of different models consistently yields better results compared to using either model alone. This empirical

Table 3: Comparison of different models.

Task	Model		Dataset	
	CLIP	Diff	MVTec-AD	VisA
Seg.	✓	×	94.7	93.7
	×	✓	95.1	96.5
	✓	✓	**95.8**	**97.3**
Cls.	✓	×	93.5	82.2
	×	✓	87.2	78.9
	✓	✓	**95.4**	**86.5**

Table 4: Comparison of different modalities.

Task	Modality		Dataset	
	Language	Vision	MVTec-AD	VisA
Seg.	✓	×	90.9	92.1
	×	✓	95.4	96.1
	✓	✓	**95.8**	**97.3**
Cls.	✓	×	93.2	79.5
	×	✓	90.5	82.8
	✓	✓	**95.4**	**86.5**

Table 5: Timestep and block configurations.

Task	Configuration	MVTec-AD	VisA
Seg.	Step ↑, Block ↑	94.3	95.1
	Step ↑, Block ↓	**95.1**	**96.5**
Cls.	Step ↑, Block ↑	86.3	76.2
	Step ↑, Block ↓	**87.2**	**78.9**

Table 6: Decoder blocks for feature maps.

Task	Early Block	MVTec-AD	VisA
Seg.	w/	94.9	93.7
	w/o	**95.1**	**96.5**
Cls.	w/	86.5	74.9
	w/o	**87.2**	**78.9**

evidence suggests that the two models capture complementary features, making their integration beneficial for both segmentation and classification tasks.

Table 4 presents the performance of different modalities, highlighting their complementary strengths through the combination of semantic and spatial information.

6.2 Extraction Strategies from Diffusion Denoisers

We explore strategies to effectively extract features from diffusion denoisers. Here, we conduct experiments using only MapDiff to see the effect more clearly.

Table 5 highlights the impact of matching timestep and block numbers when calculating $M^{\texttt{Diff},V}$ (Equation 8). Note that the decoder consists of four blocks (Block 0 to Block 3). Matching higher timesteps with lower blocks yields better performance, and vice versa (Timestep 201 → Block 3, Timestep 401 → Block 2, Timestep 801 → Block 1). This pattern reflects the intrinsic behavior of the diffusion denoiser: at higher timesteps, the denoiser interprets the input image as highly noisy and prioritizes the extraction of global features. The lower blocks, which process coarse-grained information, are particularly well-suited for this task. Using higher timesteps can be seen as a regularization strategy, as they suppress local details and highlight broader patterns.

Table 6 shows that when calculating $M^{\texttt{Diff},V}$ (Equation 8), including the early block (Block 0) does not enhance the model's performance. On the contrary, excluding this block consistently yields better results. This suggests that the early stages of the decoder act as preparatory steps for the later stages, without forming concrete features.

6.3 Inference speed

Our method can be viewed as an extension of WinCLIP (Jeong et al., 2023). We report the inference latency measured on an NVIDIA A100 GPU (40 GB) in Table 7, with a batch size of 1. As shown, our method is approximately 6–8 times faster than WinCLIP.

To capture fine-grained details, WinCLIP slides multi-scale windows over the query image, resulting in hundreds of forward passes. In contrast, our CLIP-based model utilizes patch embeddings obtained from a single forward pass. On top of this, we employ a diffusion-based model not as a denoiser for iterative generation, but as a feature extractor to capture fine-grained details. As a result, our method requires only a few forward passes in total.

Table 7: Comparison of latency (ms).

Latency [ms]	0-shot	1-shot	2-shot	4-shot
WinCLIP	4782	9514	9633	9710
CLIPFUSION	**783**	**1240**	**1269**	**1278**

6.4 One-for-all paradigm

IIPAD (Lv et al.) recently proposes a new setting for few-shot anomaly detection, termed the one-for-all paradigm. It aims to train a single unified model that can detect anomalies across multiple object categories. In this paradigm, the one-shot setting refers to using N normal images (one for each category), where N is the number of categories. Apart from this, we follow the same experimental setting as described in Section 5. Table 8 presents a comparison with IIPAD (the SOTA method under this paradigm) on the MVTec-AD dataset in the one-shot setting, where our method achieves higher performance. See Appendix A.4 for more results.

Table 8: One-for-all paradigm results.

Method	AUROC	AUPR
IIPAD	94.2	97.2
CLIPFUSION	**94.5**	**97.3**

7 Conclusion

We propose a methodology that synergistically combines discriminative and generative foundation models, leveraging their complementary strengths. As a concrete application, we introduce CLIPFUSION, which integrates CLIP and diffusion models for anomaly detection and consistently outperforms baselines in segmentation and classification across zero-shot and few-shot scenarios. This holistic use of features from discriminative and generative models may benefit the research community in tackling complex recognition tasks.

References

Dmitry Baranchuk, Ivan Rubachev, Andrey Voynov, Valentin Khrulkov, and Artem Babenko. Label-efficient semantic segmentation with diffusion models. *arXiv preprint arXiv:2112.03126*, 2021.

Paul Bergmann, Michael Fauser, David Sattlegger, and Carsten Steger. Mvtec ad–a comprehensive real-world dataset for unsupervised anomaly detection. In *Proceedings of the IEEE/CVF conference on computer vision and pattern recognition*, pp. 9592–9600, 2019.

Paul Bergmann, Michael Fauser, David Sattlegger, and Carsten Steger. Uninformed students: Student-teacher anomaly detection with discriminative latent embeddings. In *Proceedings of the IEEE/CVF conference on computer vision and pattern recognition*, pp. 4183–4192, 2020.

Tom Brown, Benjamin Mann, Nick Ryder, Melanie Subbiah, Jared D Kaplan, Prafulla Dhariwal, Arvind Neelakantan, Pranav Shyam, Girish Sastry, Amanda Askell, et al. Language models are few-shot learners. *Advances in neural information processing systems*, 33:1877–1901, 2020.

Yunkang Cao, Jiangning Zhang, Luca Frittoli, Yuqi Cheng, Weiming Shen, and Giacomo Boracchi. Adaclip: Adapting clip with hybrid learnable prompts for zero-shot anomaly detection. In *European Conference on Computer Vision*, pp. 55–72. Springer, 2024.

Hila Chefer, Shir Gur, and Lior Wolf. Generic attention-model explainability for interpreting bi-modal and encoder-decoder transformers. In *Proceedings of the IEEE/CVF International Conference on Computer Vision*, pp. 397–406, 2021.

Hila Chefer, Yuval Alaluf, Yael Vinker, Lior Wolf, and Daniel Cohen-Or. Attend-and-excite: Attention-based semantic guidance for text-to-image diffusion models. *ACM Transactions on Graphics (TOG)*, 42(4):1–10, 2023.

Ting Chen, Simon Kornblith, Mohammad Norouzi, and Geoffrey Hinton. A simple framework for contrastive learning of visual representations. In *International conference on machine learning*, pp. 1597–1607. PMLR, 2020.

Mehdi Cherti, Romain Beaumont, Ross Wightman, Mitchell Wortsman, Gabriel Ilharco, Cade Gordon, Christoph Schuhmann, Ludwig Schmidt, and Jenia Jitsev. Reproducible scaling laws for contrastive language-image learning. In *Proceedings of the IEEE/CVF Conference on Computer Vision and Pattern Recognition*, pp. 2818–2829, 2023.

Niv Cohen and Yedid Hoshen. Sub-image anomaly detection with deep pyramid correspondences. *arXiv preprint arXiv:2005.02357*, 2020.

Thomas Defard, Aleksandr Setkov, Angelique Loesch, and Romaric Audigier. Padim: a patch distribution modeling framework for anomaly detection and localization. In *International Conference on Pattern Recognition*, pp. 475–489. Springer, 2021.

Jia Deng, Wei Dong, Richard Socher, Li-Jia Li, Kai Li, and Li Fei-Fei. Imagenet: A large-scale hierarchical image database. In *2009 IEEE conference on computer vision and pattern recognition*, pp. 248–255. Ieee, 2009.

Prafulla Dhariwal and Alexander Nichol. Diffusion models beat gans on image synthesis. *Advances in neural information processing systems*, 34:8780–8794, 2021.

Alexey Dosovitskiy. An image is worth 16x16 words: Transformers for image recognition at scale. *arXiv preprint arXiv:2010.11929*, 2020.

Michael Fuest, Pingchuan Ma, Ming Gui, Johannes S Fischer, Vincent Tao Hu, and Bjorn Ommer. Diffusion models and representation learning: A survey. *arXiv preprint arXiv:2407.00783*, 2024.

Zhaopeng Gu, Bingke Zhu, Guibo Zhu, Yingying Chen, Hao Li, Ming Tang, and Jinqiao Wang. Filo: Zero-shot anomaly detection by fine-grained description and high-quality localization. In *Proceedings of the 32nd ACM International Conference on Multimedia*, pp. 2041–2049, 2024a.

Zhaopeng Gu, Bingke Zhu, Guibo Zhu, Yingying Chen, Ming Tang, and Jinqiao Wang. Anomalygpt: Detecting industrial anomalies using large vision-language models. In *Proceedings of the AAAI conference on artificial intelligence*, volume 38, pp. 1932–1940, 2024b.

Hewei Guo, Liping Ren, Jingjing Fu, Yuwang Wang, Zhizheng Zhang, Cuiling Lan, Haoqian Wang, and Xinwen Hou. Template-guided hierarchical feature restoration for anomaly detection. In *Proceedings of the IEEE/CVF International Conference on Computer Vision*, pp. 6447–6458, 2023.

Eric Hedlin, Gopal Sharma, Shweta Mahajan, Hossam Isack, Abhishek Kar, Andrea Tagliasacchi, and Kwang Moo Yi. Unsupervised semantic correspondence using stable diffusion. *Advances in Neural Information Processing Systems*, 36, 2024.

Amir Hertz, Ron Mokady, Jay Tenenbaum, Kfir Aberman, Yael Pritch, and Daniel Cohen-Or. Prompt-to-prompt image editing with cross attention control.(2022). *URL https://arxiv. org/abs/2208.01626*, 2022.

Jonathan Ho, Ajay Jain, and Pieter Abbeel. Denoising diffusion probabilistic models. *Advances in neural information processing systems*, 33:6840–6851, 2020.

Teng Hu, Jiangning Zhang, Ran Yi, Yuzhen Du, Xu Chen, Liang Liu, Yabiao Wang, and Chengjie Wang. Anomalydiffusion: Few-shot anomaly image generation with diffusion model. In *Proceedings of the AAAI conference on artificial intelligence*, volume 38, pp. 8526–8534, 2024.

Chaoqin Huang, Haoyan Guan, Aofan Jiang, Ya Zhang, Michael Spratling, and Yan-Feng Wang. Registration based few-shot anomaly detection. In *European Conference on Computer Vision*, pp. 303–319. Springer, 2022.

Gabriel Ilharco, Mitchell Wortsman, Ross Wightman, Cade Gordon, Nicholas Carlini, Rohan Taori, Achal Dave, Vaishaal Shankar, Hongseok Namkoong, John Miller, Hannaneh Hajishirzi, Ali Farhadi, and Ludwig Schmidt. Openclip, July 2021. URL https://doi.org/10.5281/zenodo.5143773.

Jongheon Jeong, Yang Zou, Taewan Kim, Dongqing Zhang, Avinash Ravichandran, and Onkar Dabeer. Winclip: Zero-/few-shot anomaly classification and segmentation. In *Proceedings of the IEEE/CVF Conference on Computer Vision and Pattern Recognition*, pp. 19606–19616, 2023.

Dongsheng Jiang, Yuchen Liu, Songlin Liu, Jin'e Zhao, Hao Zhang, Zhen Gao, Xiaopeng Zhang, Jin Li, and Hongkai Xiong. From clip to dino: Visual encoders shout in multi-modal large language models. *arXiv preprint arXiv:2310.08825*, 2023.

Alexander C Li, Mihir Prabhudesai, Shivam Duggal, Ellis Brown, and Deepak Pathak. Your diffusion model is secretly a zero-shot classifier. In *Proceedings of the IEEE/CVF International Conference on Computer Vision*, pp. 2206–2217, 2023a.

Chun-Liang Li, Kihyuk Sohn, Jinsung Yoon, and Tomas Pfister. Cutpaste: Self-supervised learning for anomaly detection and localization. In *Proceedings of the IEEE/CVF conference on computer vision and pattern recognition*, pp. 9664–9674, 2021.

Xiaofan Li, Zhizhong Zhang, Xin Tan, Chengwei Chen, Yanyun Qu, Yuan Xie, and Lizhuang Ma. Promptad: Learning prompts with only normal samples for few-shot anomaly detection. In *Proceedings of the IEEE/CVF Conference on Computer Vision and Pattern Recognition*, pp. 16838–16848, 2024a.

Xurui Li, Ziming Huang, Feng Xue, and Yu Zhou. Musc: Zero-shot industrial anomaly classification and segmentation with mutual scoring of the unlabeled images. *arXiv preprint arXiv:2401.16753*, 2024b.

Yi Li, Hualiang Wang, Yiqun Duan, and Xiaomeng Li. Clip surgery for better explainability with enhancement in open-vocabulary tasks. *arXiv preprint arXiv:2304.05653*, 2023b.

Yiyue Li, Shaoting Zhang, Kang Li, and Qicheng Lao. One-to-normal: Anomaly personalization for few-shot anomaly detection. *Advances in Neural Information Processing Systems*, 37:78371–78393, 2024c.

Bingyan Liu, Chengyu Wang, Tingfeng Cao, Kui Jia, and Jun Huang. Towards understanding cross and self-attention in stable diffusion for text-guided image editing. In *Proceedings of the IEEE/CVF Conference on Computer Vision and Pattern Recognition*, pp. 7817–7826, 2024.

Wenxi Lv, Qinliang Su, and Wenchao Xu. One-for-all few-shot anomaly detection via instance-induced prompt learning. In *The Thirteenth International Conference on Learning Representations*.

Bjoern H Menze, Andras Jakab, Stefan Bauer, Jayashree Kalpathy-Cramer, Keyvan Farahani, Justin Kirby, Yuliya Burren, Nicole Porz, Johannes Slotboom, Roland Wiest, et al. The multimodal brain tumor image segmentation benchmark (brats). *IEEE transactions on medical imaging*, 34(10):1993–2024, 2014.

Alexander Quinn Nichol and Prafulla Dhariwal. Improved denoising diffusion probabilistic models. In *International conference on machine learning*, pp. 8162–8171. PMLR, 2021.

Zhen Qu, Xian Tao, Mukesh Prasad, Fei Shen, Zhengtao Zhang, Xinyi Gong, and Guiguang Ding. Vcp-clip: A visual context prompting model for zero-shot anomaly segmentation. In *European Conference on Computer Vision*, pp. 301–317. Springer, 2024.

Alec Radford, Jong Wook Kim, Chris Hallacy, Aditya Ramesh, Gabriel Goh, Sandhini Agarwal, Girish Sastry, Amanda Askell, Pamela Mishkin, Jack Clark, et al. Learning transferable visual models from natural language supervision. In *International conference on machine learning*, pp. 8748–8763. PMLR, 2021.

Aditya Ramesh, Mikhail Pavlov, Gabriel Goh, Scott Gray, Chelsea Voss, Alec Radford, Mark Chen, and Ilya Sutskever. Zero-shot text-to-image generation. In *International conference on machine learning*, pp. 8821–8831. Pmlr, 2021.

Aditya Ramesh, Prafulla Dhariwal, Alex Nichol, Casey Chu, and Mark Chen. Hierarchical text-conditional image generation with clip latents. *arXiv preprint arXiv:2204.06125*, 1(2):3, 2022.

Robin Rombach, Andreas Blattmann, Dominik Lorenz, Patrick Esser, and Björn Ommer. High-resolution image synthesis with latent diffusion models, 2021.

Robin Rombach, Andreas Blattmann, Dominik Lorenz, Patrick Esser, and Björn Ommer. High-resolution image synthesis with latent diffusion models. In *Proceedings of the IEEE/CVF Conference on Computer Vision and Pattern Recognition (CVPR)*, pp. 10684–10695, June 2022.

Olaf Ronneberger, Philipp Fischer, and Thomas Brox. U-net: Convolutional networks for biomedical image segmentation. In *Medical image computing and computer-assisted intervention–MICCAI 2015: 18th international conference, Munich, Germany, October 5-9, 2015, proceedings, part III 18*, pp. 234–241. Springer, 2015.

Karsten Roth, Latha Pemula, Joaquin Zepeda, Bernhard Schölkopf, Thomas Brox, and Peter Gehler. Towards total recall in industrial anomaly detection. In *Proceedings of the IEEE/CVF conference on computer vision and pattern recognition*, pp. 14318–14328, 2022.

Marco Rudolph, Bastian Wandt, and Bodo Rosenhahn. Same same but differnet: Semi-supervised defect detection with normalizing flows. In *Proceedings of the IEEE/CVF winter conference on applications of computer vision*, pp. 1907–1916, 2021.

Christoph Schuhmann, Richard Vencu, Romain Beaumont, Robert Kaczmarczyk, Clayton Mullis, Aarush Katta, Theo Coombes, Jenia Jitsev, and Aran Komatsuzaki. Laion-400m: Open dataset of clip-filtered 400 million image-text pairs. *arXiv preprint arXiv:2111.02114*, 2021.

Christoph Schuhmann, Romain Beaumont, Richard Vencu, Cade W Gordon, Ross Wightman, Mehdi Cherti, Theo Coombes, Aarush Katta, Clayton Mullis, Mitchell Wortsman, Patrick Schramowski, Srivatsa R Kundurthy, Katherine Crowson, Ludwig Schmidt, Robert Kaczmarczyk, and Jenia Jitsev. LAION-5b: An open large-scale dataset for training next generation image-text models. In *Thirty-sixth Conference on Neural Information Processing Systems Datasets and Benchmarks Track*, 2022. URL https://openreview.net/forum?id=M3Y74vmsMcY.

Arnaud Arindra Adiyoso Setio, Alberto Traverso, Thomas De Bel, Moira SN Berens, Cas Van Den Bogaard, Piergiorgio Cerello, Hao Chen, Qi Dou, Maria Evelina Fantacci, Bram Geurts, et al. Validation, comparison, and combination of algorithms for automatic detection of pulmonary nodules in computed tomography images: the luna16 challenge. *Medical image analysis*, 42:1–13, 2017.

Shelly Sheynin, Sagie Benaim, and Lior Wolf. A hierarchical transformation-discriminating generative model for few shot anomaly detection. In *Proceedings of the IEEE/CVF international conference on computer vision*, pp. 8495–8504, 2021.

Yang Song, Jascha Sohl-Dickstein, Diederik P Kingma, Abhishek Kumar, Stefano Ermon, and Ben Poole. Score-based generative modeling through stochastic differential equations. *arXiv preprint arXiv:2011.13456*, 2020.

Patrick von Platen, Suraj Patil, Anton Lozhkov, Pedro Cuenca, Nathan Lambert, Kashif Rasul, Mishig Davaadorj, Dhruv Nair, Sayak Paul, William Berman, Yiyi Xu, Steven Liu, and Thomas Wolf. Diffusers: State-of-the-art diffusion models. https://github.com/huggingface/diffusers, 2022.

Monika Wysoczańska, Oriane Siméoni, Michaël Ramamonjisoa, Andrei Bursuc, Tomasz Trzciński, and Patrick Pérez. Clip-dinoiser: Teaching clip a few dino tricks for open-vocabulary semantic segmentation. In *European Conference on Computer Vision*, pp. 320–337. Springer, 2025.

Xincheng Yao, Zixin Chen, Chao Gao, Guangtao Zhai, and Chongyang Zhang. Resad: A simple framework for class generalizable anomaly detection. *Advances in Neural Information Processing Systems*, 37:125287–125311, 2024.

Vitjan Zavrtanik, Matej Kristan, and Danijel Skočaj. Draem-a discriminatively trained reconstruction embedding for surface anomaly detection. In *Proceedings of the IEEE/CVF international conference on computer vision*, pp. 8330–8339, 2021.

Xinyi Zhang, Naiqi Li, Jiawei Li, Tao Dai, Yong Jiang, and Shu-Tao Xia. Unsupervised surface anomaly detection with diffusion probabilistic model. In *Proceedings of the IEEE/CVF International Conference on Computer Vision*, pp. 6782–6791, 2023a.

Xujie Zhang, Binbin Yang, Michael C Kampffmeyer, Wenqing Zhang, Shiyue Zhang, Guansong Lu, Liang Lin, Hang Xu, and Xiaodan Liang. Diffcloth: Diffusion based garment synthesis and manipulation via structural cross-modal semantic alignment. In *Proceedings of the IEEE/CVF International Conference on Computer Vision*, pp. 23154–23163, 2023b.

Wenliang Zhao, Yongming Rao, Zuyan Liu, Benlin Liu, Jie Zhou, and Jiwen Lu. Unleashing text-to-image diffusion models for visual perception. In *Proceedings of the IEEE/CVF International Conference on Computer Vision*, pp. 5729–5739, 2023.

Chong Zhou, Chen Change Loy, and Bo Dai. Extract free dense labels from clip. In *European Conference on Computer Vision*, pp. 696–712. Springer, 2022.

Qihang Zhou, Guansong Pang, Yu Tian, Shibo He, and Jiming Chen. Anomalyclip: Object-agnostic prompt learning for zero-shot anomaly detection. *arXiv preprint arXiv:2310.18961*, 2023.

Jiawen Zhu and Guansong Pang. Toward generalist anomaly detection via in-context residual learning with few-shot sample prompts. In *Proceedings of the IEEE/CVF conference on computer vision and pattern recognition*, pp. 17826–17836, 2024.

Yang Zou, Jongheon Jeong, Latha Pemula, Dongqing Zhang, and Onkar Dabeer. Spot-the-difference self-supervised pre-training for anomaly detection and segmentation. In *European Conference on Computer Vision*, pp. 392–408. Springer, 2022.

A Appendix

A.1 Further motivation for feature-based anomaly detection

Addressing anomaly detection with a single-perspective approach is challenging due to the open-ended nature of abnormality. Discriminative models focus on global features but often miss fine-grained details, which are crucial for detecting local structural or textural anomalies.

When utilizing generative models in anomaly detection, the reconstruction-based approach has traditionally been the dominant paradigm (Zavrtanik et al., 2021; Zhang et al., 2023a; Guo et al., 2023). This approach compares the original image and the reconstructed image at both ends. However, since generative models are primarily designed for creative image generation, they can produce high reconstruction errors even for normal images. In addition, deciding how to apply the mask, including its location and size is challenging.[4] As a result, the feature-based approach has recently gained prominence.

[4]Since the location of the anomalous part is not known, it is unclear where to apply the mask. Also, if the mask is too large, the reconstructed image may deviate significantly from the original image. Conversely, if the mask is too small and fails to fully cover the anomaly, the anomaly may persist or even extend in the reconstructed image.

Building on this shift, we propose that a more fundamental approach to utilizing generative models for anomaly detection is to extract features midway through the process. This leverages the image understanding capability that underlies their image generation capability.

A.2 Further experimental details

Data pre-processing For PatchCLIP, we use the same pre-processing pipeline as in WinCLIP (Jeong et al., 2023), which is specified in OpenCLIP (Ilharco et al., 2021), for both MVTec-AD and VisA datasets. First, bicubic interpolation is used to resize images to a resolution of 240 to fit the ViT-B-16-plus-240 model. After which, channel-wise standardization is applied with the precomputed values of (0.48145466, 0.4578275, 0.40821073) for the mean and (0.26862954, 0.26130258, 0.27577711) for the standard deviation. For MapDiff, we use bilinear interpolation to resize images to a resolution of 512 before feeding into a customized Stable Diffusion Inpainting pipeline from the diffusers library (von Platen et al., 2022).

Prompts The prompts are derived from those used to train CLIP for the ImageNet dataset (Deng et al., 2009). For example, in the case of a segmentation task on MVTec-AD, PatchCLIP uses the prompt "`a good, cropped picture of the [state] [object] for classification`", where `[state]` is either "`damaged`" or "`perfect`". MapDiff uses the prompt "`a close-up cropped png photo of a [object] with [state] for anomaly segmentation`" for query images. The `[state]` includes commonly observed anomaly types "`crack`", "`hole`", and "`residue`", along with a generic descriptor "`damage`". For reference images, it uses the prompt "`a photo of a perfect [object]`".

Evaluation metrics We follow previous studies (Cohen & Hoshen, 2020; Defard et al., 2021; Roth et al., 2022; Jeong et al., 2023) and use the following performance metrics. For anomaly classification, we report the Area Under the ROC Curve (AUROC) at the image level and the Area Under the Precision-Recall Curve (AUPR). For anomaly segmentation, we report the AUROC at the pixel level and the Area Under the Per-Region Overlap Curve (AUPRO) (Bergmann et al., 2020; Li et al., 2021). Both AUPR and AUPRO are particularly sensitive to class imbalance.

Hyperparameters We compare weights of (1, 0), (0, 1), (0.75, 0.25), (0.25, 0.75), and (0.5, 0.5) between the CLIP and diffusion models. We observe a consistent trend: (0.25, 0.75) is effective for segmentation tasks, while (0.75, 0.25) performs better for classification tasks. The same weights are used across all datasets for each task. Please refer to Table 3.

Baseline performance The performance of Trans-MM, MaskCLIP, PaDiM, PatchCore, CLIP-AC, and WinCLIP are referenced from the WinCLIP paper (Jeong et al., 2023).

A.3 Further empirical study

Table 9 demonstrates the effectiveness of extracting cross-attention maps from the encoder (down-blocks) and decoder (up-blocks) while excluding the bottleneck (mid-block). Integrating the bottleneck results in suboptimal performance due to its lack of spatial granularity critical for tasks like anomaly detection.

Table 9: Denoiser components for cross-attention maps.

Task	Denoiser Component			Dataset	
	Enc	Bneck	Dec	MVTec-AD	VisA
Seg.	×	×	✓	94.4	96.0
	✓	✓	✓	94.4	96.4
	✓	×	✓	**95.1**	**96.5**
Cls.	×	×	✓	83.2	74.1
	✓	✓	✓	86.8	76.1
	✓	×	✓	**87.2**	**78.9**

Table 10 illustrates the impact of using state ensemble for a cross-attention map. Without ensemble, only a generic term "`damage`" is used to generate the cross-attention map. In contrast, the ensemble approach averages cross-attention maps derived from both the generic term "`damage`" and more specific terms such as "`crack`," "`hole`," and "`residue`." This approach significantly improves performance across tasks. By incorporating these multiple specific states, the method generates diverse cross-attention maps that capture fine-grained and complementary aspects of anomalies.

Table 10: State ensemble (generic and specific).

Task	Ensemble	Dataset	
		MVTec-AD	VisA
Seg.	w/o	94.0	95.8
	w/	**95.1**	**96.5**
Cls.	w/o	85.4	73.1
	w/	**87.2**	**78.9**

Table 11 shows the impact of customizing state descriptors for each object class on performance. For example, for both Cable and Pill, replacing the default set of states with a class-specific set composed of frequently occurring anomaly types leads to consistent performance improvements.

Table 11: Effect of state customization.

Object	State Set	AUROC
Cable	"`crack`", "`hole`", "`residue`", "`damage`"	94.6
	"`crack`", "`poke`", "`scratch`"	**95.0**
Pill	"`crack`", "`hole`", "`residue`", "`damage`"	83.0
	"`crack`", "`scratch`", "`residue`"	**83.5**

Table 12 presents results obtained with different sets of states. The results show our method remains reasonably robust across these variations.

Table 12: Different sets of states.

States	Task	Dataset	
		MVTec-AD	VisA
"`contamination`", "`bend`", "`cut`", "`damage`"	Seg.	95.8	97.0
	Cls.	95.4	85.9
"`break`", "`fold`", "`stain`", "`damage`"	Seg.	95.8	97.3
	Cls.	95.6	86.1

A.4 Further results in the one-for-all paradigm

We evaluate anomaly detection performance under the one-for-all paradigm, where a single model is applied across all object categories. Recall that, in this paradigm, the one-shot setting provides one image per category, for a total of N images across N object categories. IIPAD (Lv et al.) trains a prompt generator using these examples for the one-for-all setting. In contrast, CLIPFUSION requires no additional training. Nevertheless, it outperforms or matches IIPAD across all configurations and datasets for both segmentation and classification, as shown in Tables 13 and 14.

A.5 Limitations of few-shot training

Training-based methods inherently suffer from epoch selection sensitivity. Figure 4a shows that the epoch at which PromptAD performs best differs significantly across object categories. In conventional training setups,

Table 13: Quantitative results for anomaly segmentation in the one-for-all paradigm.

Setup	Method	MVTec-AD		VisA	
		AUROC	AUPR	AUROC	AUPR
1-shot	IIPAD	**96.4**	89.8	96.9	**87.3**
	CLIPFUSION	96.0	**91.1**	**97.2**	**87.3**
2-shot	IIPAD	**96.7**	90.3	97.2	87.9
	CLIPFUSION	96.4	**91.9**	**97.4**	**88.1**
4-shot	IIPAD	**97.0**	91.2	97.4	88.3
	CLIPFUSION	96.8	**92.5**	**98.1**	**88.6**

Table 14: Quantitative results for anomaly classification in the one-for-all paradigm.

Setup	Method	MVTec-AD		VisA	
		AUROC	AUPR	AUROC	AUPR
1-shot	IIPAD	94.2	97.2	85.4	87.5
	CLIPFUSION	**94.5**	**97.3**	**85.5**	**88.1**
2-shot	IIPAD	95.7	**97.9**	86.7	88.6
	CLIPFUSION	**96.0**	**97.9**	**86.8**	**89.3**
4-shot	IIPAD	96.1	98.1	**88.3**	89.6
	CLIPFUSION	**96.4**	**98.2**	**88.3**	**90.0**

such epoch selection is guided by a validation set. However, in few-shot anomaly detection, where only one to four images are available, it is practically hard to reserve any for a separate validation set. The authors of PromptAD circumvent this by using the test set for validation in their official implementation.[5] However, test sets are not accessible during model training in real-world applications. In contrast, CLIPFUSION requires no additional training and uses few-shot examples solely for feature extraction, making validation sets and epoch selection unnecessary.

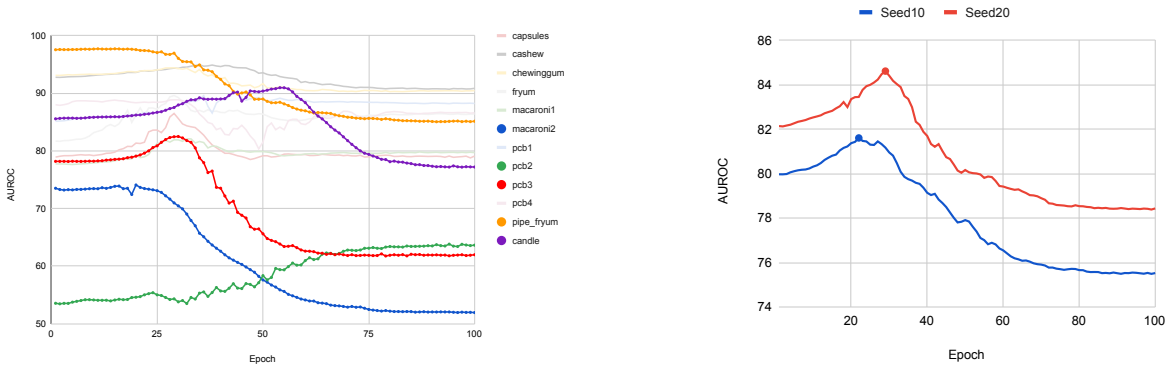

(a) AUROC for individual objects.

(b) Average AUROC over all objects.

Figure 4: AUROC across training epochs on the VisA dataset (1-shot setting).

Figure 4b reveals that even when the training epoch is fixed, performance varies considerably across different random seeds. This highlights the instability and seed sensitivity of few-shot training, making it difficult to ensure consistent and reproducible results without a validation set.

[5] https://github.com/FuNz-0/PromptAD

A.6 Effect of weights between the CLIP and diffusion models

We analyze the effect of varying the weights assigned to the CLIP and diffusion models. Recall that α and $(1-\alpha)$ denote the weights of the CLIP and the diffusion model, respectively. By changing α, we adjust their relative contributions and evaluate the performance. As shown in Table 15, segmentation achieves the best performance among the tested alpha values at $\alpha = 0.25$, while classification performed best at $\alpha = 0.75$.

Table 15: Effect of weights on performance.

Task	Weight		Dataset	
	CLIP	Diff	MVTec-AD	VisA
Seg.	1	0	94.7	93.7
	0.75	0.25	95.4	96.1
	0.5	0.5	95.7	97.2
	0.25	0.75	**95.8**	**97.3**
	0	1	95.1	96.5
Cls.	1	0	93.5	82.2
	0.75	0.25	**95.4**	**86.5**
	0.5	0.5	95.0	86.4
	0.25	0.75	92.7	83.9
	0	1	87.2	78.9

A.7 Failure cases

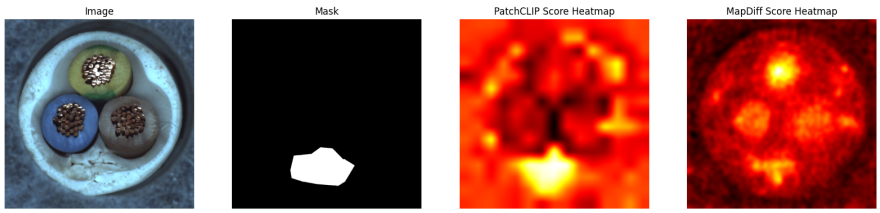

(a) Attention saturation (Cable)

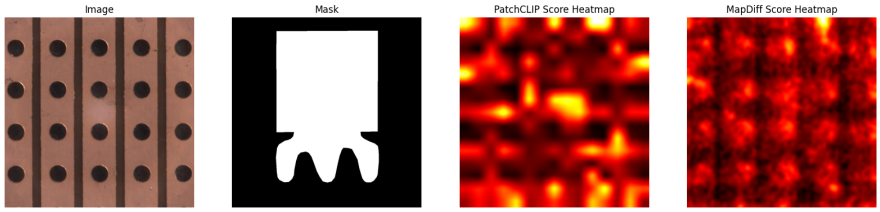

(b) Logical anomaly (Transistor)

Figure 5: Failure analysis examples.

Figure 5 provides representative failure cases. In Figure 5(a), although the anomaly lies in the outer sheath of the cables, the diffusion-based model over-activates on the dense and repetitive wire patterns, failing to highlight the true defect. Figure 5(b) shows a logical anomaly, where the absence of a transistor itself constitutes the defect. Lacking this contextual understanding, the models struggle to determine where to attend, resulting in mislocalization.

A.8 Results on different backbones

Table 16 reports the performance of our framework with different diffusion backbones. We observe that the results are consistent across backbones. This indicates that our method is robust to the choice of diffusion backbone.

Table 16: Different backbones.

Backbone	Task	Dataset	
		MVTec-AD	VisA
Stable Diffusion v1.5	Seg.	95.8	96.7
	Cls.	93.5	86.4
Stable Diffusion v2.0	Seg.	95.8	97.3
	Cls.	95.4	86.5
Stable Diffusion v2.1	Seg.	95.8	97.3
	Cls.	94.6	86.5

A.9 Pseudocode

Algorithm 1 CLIPFUSION for Anomaly **Segmentation**

Require: Query image x; optional k normal reference images $\mathcal{R} = \{r_i\}_{i=1}^{k}$; object label o; state set $\mathcal{C}$; CLIP image and text encoders f_I, f_T; diffusion denoiser ϵ_θ; CLIP blocks $\mathcal{B}$; Diffusion timestep-block pairs $\mathcal{T} = \{(t, b)\}$; fusion weight $\alpha \in [0, 1]$

Ensure: Pixel-level anomaly map M

Initialize $M^{\texttt{CLIP},L}, M^{\texttt{Diff},L} \leftarrow 0$ ▷ See Sec. 4.1.1 zero-shot
(CLIP, language-guided)
Encode x with f_I to obtain the patch embeddings
Encode prompts "a photo of the perfect [o]" and "a photo of the damaged [o]" with f_T
Form $M^{\texttt{CLIP},L}$ by per-patch alignment (abnormal vs. normal)
(Diffusion, language-guided)
for state $s \in \mathcal{C}$ **do**
  Run ϵ_θ on x with empty mask and prompt "a photo of a [o] with [s]"
  Extract cross-attention map for state s; accumulate $M^{\texttt{Diff},L} \leftarrow M^{\texttt{Diff},L} + \text{CrossAttn}(s)$
end for
$M^{\texttt{Diff},L} \leftarrow M^{\texttt{Diff},L}/|\mathcal{C}|$

Initialize $M^{\texttt{CLIP},V}, M^{\texttt{Diff},V} \leftarrow 0$ ▷ See Sec. 4.1.2 few-shot
if $k > 0$ **then**
  (CLIP, vision-guided)
  For each $r \in \mathcal{R}$ and $b \in \mathcal{B}$, extract features from f_I and store into $\mathcal{R}^b$
  For each (h, w),
    $M^{\texttt{CLIP},V}_{h,w} \leftarrow \frac{1}{|\mathcal{B}|} \sum_{b \in \mathcal{B}} \min_{r \in \mathcal{R}^b} \frac{1}{2} \left(1 - \text{sim}(F^b_{h,w}, r)\right)$ (Eq. 7)
  (Diffusion, vision-guided)
  For each $r \in \mathcal{R}$ and $(t, b) \in \mathcal{T}$, extract features from ϵ_θ and store into $\mathcal{R}^{t,b}$
  For each (h, w),
    $M^{\texttt{Diff},V}_{h,w} \leftarrow \frac{1}{|\mathcal{T}|} \sum_{(t,b) \in \mathcal{T}} \min_{r \in \mathcal{R}^{t,b}} \frac{1}{2} \left(1 - \text{sim}(F^{t,b}_{h,w}, r)\right)$ (Eq. 8)
end if
Fuse maps $M \leftarrow \alpha(M^{\texttt{CLIP},L} + M^{\texttt{CLIP},V}) + (1 - \alpha)(M^{\texttt{Diff},L} + M^{\texttt{Diff},V})$ (Eq. 4)
return M

Algorithm 2 CLIPFUSION for Anomaly **Classification**

Require: Query image x; optional k normal reference images $\mathcal{R} = \{r_i\}_{i=1}^{k}$; object label o; state set $\mathcal{C}$; CLIP image and text encoders f_I, f_T; diffusion denoiser ϵ_θ; CLIP blocks $\mathcal{B}$; Diffusion timestep–block pairs $\mathcal{T} = \{(t, b)\}$; fusion weight $\alpha \in [0, 1]$

Ensure: Image-level anomaly score S

Initialize $S^{\texttt{CLIP},L}, S^{\texttt{Diff},L} \leftarrow 0$ ▷ See Sec. 4.2
(CLIP, language-guided)
Encode x with f_I to obtain the class token embedding
Encode prompts "a photo of the perfect [o]" and "a photo of the damaged [o]" with f_T
Calculate $S^{\texttt{CLIP},L}$ via Eq. (1)
(Diffusion, language-guided)
Compute $M^{\texttt{Diff},L}$ as in Alg. 1
$S^{\texttt{Diff},L} \leftarrow 1 - \text{median}(M^{\texttt{Diff},L}) / \max(M^{\texttt{Diff},L})$ (Eq. 10)

Initialize $S^{\texttt{CLIP},V}, S^{\texttt{Diff},V} \leftarrow 0$
if $k > 0$ **then**
    (CLIP, vision-guided)
    Build memory banks $\mathcal{R}^b$ from f_I; compute $M^{\texttt{CLIP},V}$ as in Alg. 1
    $S^{\texttt{CLIP},V} \leftarrow \max(M^{\texttt{CLIP},V})$ (Eq. 11)
    (Diffusion, vision-guided)
    Build memory banks $\mathcal{R}^{t,b}$ from ϵ_θ; compute $M^{\texttt{Diff},V}$ as in Alg. 1
    $S^{\texttt{Diff},V} \leftarrow \max(M^{\texttt{Diff},V})$ (Eq. 11)
end if
Fuse scores $S \leftarrow \alpha\big(S^{\texttt{CLIP},L} + S^{\texttt{CLIP},V}\big) + (1-\alpha)\big(S^{\texttt{Diff},L} + S^{\texttt{Diff},V}\big)$ (Eq. 9)
return S

A.10 Detailed quantitative results

Table 17: AUROC (%) results on MVTec-AD classification.

Category	k=0		k=1				k=2				k=4			
	WinCLIP	CLIPFUSION	PaDiM	PatchCore	WinCLIP	CLIPFUSION	PaDiM	PatchCore	WinCLIP	CLIPFUSION	PaDiM	PatchCore	WinCLIP	CLIPFUSION
Bottle	99.2±0.0	100.0±0.0	97.4±0.7	99.4±0.4	98.2±0.9	100.0±0.0	98.5±1.0	99.2±0.3	99.3±0.3	100.0±0.0	98.8±0.2	99.2±0.3	99.3±0.4	100.0±0.0
Cable	86.5±0.0	87.3±0.0	57.7±4.6	88.8±4.2	88.9±1.9	95.0±0.9	62.3±5.9	91.0±2.7	88.4±0.7	96.3±0.4	70.0±6.1	91.0±2.7	90.9±0.9	96.7±0.4
Capsule	72.9±0.0	88.1±0.0	57.7±7.3	67.8±2.9	72.3±6.8	83.6±6.9	64.3±3.0	72.8±7.0	77.3±8.8	89.0±2.7	65.2±2.5	72.8±7.0	82.3±8.9	91.2±1.6
Carpet	100.0±0.0	99.9±0.0	96.6±1.0	95.3±0.8	99.8±0.3	100.0±0.0	97.8±0.5	96.6±0.5	99.8±0.3	100.0±0.1	97.9±0.4	96.6±0.5	100.0±0.0	100.0±0.0
Grid	98.8±0.0	99.9±0.0	54.2±6.7	63.6±10.3	99.5±0.3	99.4±0.4	67.2±4.2	67.7±8.3	99.4±0.2	99.6±0.4	68.1±3.8	67.7±8.3	99.6±0.1	99.5±0.4
Hazelnut	93.9±0.0	96.9±0.0	88.3±2.6	88.3±2.7	97.5±1.4	99.3±0.4	90.8±0.8	93.2±3.8	98.3±0.7	99.3±0.3	91.9±1.2	93.2±3.8	98.4±0.4	99.3±0.5
Leather	100.0±0.0	99.9±0.0	97.5±0.7	97.3±0.7	99.9±0.0	99.9±0.0	97.5±0.9	97.9±0.7	99.9±0.0	100.0±0.0	98.5±0.2	97.9±0.7	100.0±0.0	100.0±0.0
Metal nut	97.1±0.0	98.3±0.0	53.0±3.8	73.4±2.9	98.7±0.8	99.8±0.3	54.8±3.8	77.7±8.5	99.4±0.2	99.9±0.2	60.7±5.2	77.7±8.5	99.5±0.2	100.0±0.0
Pill	79.1±0.0	77.6±0.0	61.3±3.8	81.9±2.8	91.2±2.1	96.1±0.4	59.1±6.4	82.9±2.9	92.3±0.7	96.2±0.2	54.9±2.7	82.9±2.9	92.8±1.0	96.4±0.4
Screw	83.3±0.0	77.3±0.0	55.0±2.5	44.4±4.6	86.4±0.9	72.5±8.5	54.0±4.4	49.0±3.8	86.0±2.1	73.5±5.1	50.0±4.1	49.0±3.8	87.9±1.2	82.0±4.5
Tile	100.0±0.0	99.1±0.0	92.2±2.2	99.0±0.9	99.9±0.0	99.9±0.2	93.3±1.1	98.5±1.0	99.9±0.2	99.9±0.1	93.1±0.6	98.5±1.0	99.9±0.1	100.0±0.0
Toothbrush	87.5±0.0	96.9±0.0	82.5±1.2	83.3±3.8	92.2±4.9	98.9±1.6	87.6±4.2	85.9±3.5	97.5±1.6	99.1±0.8	89.2±2.5	85.9±3.5	96.7±2.6	98.5±0.8
Transistor	88.0±0.0	86.7±0.0	73.3±6.0	78.1±6.9	83.4±3.8	90.9±1.4	72.8±6.3	90.0±4.3	85.3±1.7	91.1±0.8	82.4±6.5	90.0±4.3	85.7±2.5	92.9±1.0
Wood	99.4±0.0	96.7±0.0	96.1±1.2	97.8±0.3	99.9±0.1	98.9±0.3	96.9±0.5	98.3±0.6	99.9±0.1	98.6±0.2	97.0±0.2	98.3±0.6	99.8±0.3	98.8±0.1
Zipper	91.5±0.0	94.0±0.0	85.8±2.7	92.3±0.5	88.8±5.9	96.5±0.7	86.3±2.6	94.0±2.1	94.0±1.4	95.3±2.2	88.3±2.0	94.0±2.1	94.5±0.5	96.2±0.6
Mean	91.8±0.0	**93.2±0.0**	76.6±3.1	83.4±3.0	93.1±2.0	**95.4±0.8**	78.9±3.1	86.3±3.3	94.4±1.3	**95.9±0.3**	80.4±2.5	88.8±2.6	95.2±1.3	**96.8±0.2**

Table 18: AUPR (%) results on MVTec-AD classification.

Category	k=0		k=1				k=2				k=4			
	WinCLIP	CLIPFUSION	PaDiM	PatchCore	WinCLIP	CLIPFUSION	PaDiM	PatchCore	WinCLIP	CLIPFUSION	PaDiM	PatchCore	WinCLIP	CLIPFUSION
Bottle	99.8±0.0	100.0±0.0	99.2±0.2	99.8±0.1	99.4±0.3	100.0±0.0	99.6±0.3	99.8±0.1	99.8±0.1	100.0±0.0	99.7±0.0	99.8±0.1	99.8±0.1	100.0±0.0
Cable	91.2±0.0	92.7±0.0	64.9±3.8	93.8±2.2	93.2±1.1	97.1±0.5	69.6±6.6	95.1±1.3	92.9±0.6	97.8±0.3	76.1±5.6	97.1±0.7	94.4±0.3	98.1±0.2
Capsule	91.5±0.0	97.2±0.0	86.9±2.2	89.4±2.0	91.6±2.7	95.9±2.2	88.4±0.8	91.0±2.9	93.3±3.6	97.4±0.8	87.8±0.8	94.9±1.1	95.1±3.3	98.0±0.4
Carpet	100.0±0.0	100.0±0.0	99.0±0.2	98.7±0.2	99.9±0.1	100.0±0.0	99.4±0.1	99.0±0.1	99.9±0.1	100.0±0.0	99.4±0.1	98.8±0.2	100.0±0.0	100.0±0.0
Grid	99.6±0.0	100.0±0.0	75.0±3.3	81.1±4.9	99.9±0.1	99.8±0.1	82.5±2.3	84.1±4.0	99.8±0.1	99.9±0.1	83.0±1.8	86.4±4.0	99.9±0.0	99.8±0.1
Hazelnut	96.9±0.0	98.3±0.0	93.3±1.7	92.9±2.2	98.6±0.7	99.6±0.2	94.1±0.5	96.0±2.0	99.1±0.4	99.6±0.1	94.8±0.6	97.0±1.2	99.1±0.2	99.6±0.3
Leather	100.0±0.0	100.0±0.0	99.2±0.2	99.1±0.2	100.0±0.0	100.0±0.0	99.2±0.3	99.3±0.2	100.0±0.0	100.0±0.0	99.6±0.1	99.6±0.1	100.0±0.0	100.0±0.0
Metal nut	99.3±0.0	99.6±0.0	82.0±2.7	91.0±1.1	99.7±0.2	99.9±0.1	82.2±1.4	92.3±4.0	99.9±0.0	100.0±0.0	85.5±1.7	97.0±2.6	99.9±0.1	100.0±0.0
Pill	95.7±0.0	94.8±0.0	88.3±1.3	96.5±0.6	98.3±0.5	99.3±0.1	87.9±2.6	96.6±0.7	98.6±0.1	99.3±0.0	87.0±1.2	96.9±0.4	98.6±0.2	99.4±0.1
Screw	93.1±0.0	89.3±0.0	78.1±1.0	71.4±2.3	94.2±0.6	87.5±4.7	77.3±1.3	72.9±3.4	94.1±1.5	87.4±3.2	75.7±2.8	71.8±1.9	94.9±0.8	93.0±2.3
Tile	100.0±0.0	99.6±0.0	97.2±0.7	99.6±0.3	100.0±0.0	100.0±0.1	97.6±0.4	99.4±0.4	100.0±0.1	100.0±0.0	97.6±0.2	99.6±0.1	100.0±0.0	100.0±0.0
Toothbrush	95.6±0.0	98.8±0.0	93.7±0.5	93.5±1.4	96.7±2.0	99.6±0.5	95.2±1.6	94.1±1.4	99.0±0.6	99.7±0.3	95.8±0.7	94.8±0.7	98.7±1.1	99.5±0.2
Transistor	87.1±0.0	84.7±0.0	66.2±7.5	77.7±5.5	79.0±4.0	89.8±1.5	69.0±6.5	89.3±3.9	80.7±2.3	89.9±0.7	77.6±8.4	84.5±9.0	80.7±3.2	92.3±1.3
Wood	99.8±0.0	99.0±0.0	98.8±0.3	99.3±0.1	100.0±0.0	99.7±0.1	99.0±0.1	99.5±0.2	100.0±0.0	99.6±0.1	99.1±0.0	99.5±0.2	99.9±0.1	99.7±0.0
Zipper	97.5±0.0	97.9±0.0	95.5±0.9	97.2±0.3	96.8±1.8	98.9±0.3	95.4±1.0	97.8±1.0	98.3±0.4	98.3±1.0	96.2±0.8	99.1±0.7	98.5±0.2	98.7±0.2
Mean	96.5±0.0	**96.8±0.0**	88.1±1.7	92.2±1.5	96.5±0.9	**97.8±0.4**	89.3±1.7	93.8±1.7	97.0±0.7	**97.9±0.2**	90.5±1.6	94.5±1.5	97.3±0.6	**98.5±0.1**

Table 19: AUROC (%) results on MVTec-AD segmentation.

Category	k=0		k=1				k=2				k=4			
	WinCLIP	CLIPFUSION	PaDiM	PatchCore	WinCLIP	CLIPFUSION	PaDiM	PatchCore	WinCLIP	CLIPFUSION	PaDiM	PatchCore	WinCLIP	CLIPFUSION
Bottle	89.5±0.0	94.1±0.0	96.1±0.5	97.9±0.1	97.5±0.2	97.3±0.2	96.9±0.1	98.1±0.0	97.7±0.1	97.5±0.0	97.1±0.1	98.2±0.0	97.8±0.0	97.7±0.1
Cable	77.0±0.0	73.2±0.0	88.4±1.2	95.5±0.8	93.8±0.6	91.3±0.2	90.0±0.8	96.4±0.3	94.3±0.4	92.2±0.3	92.1±0.4	97.5±0.3	94.9±0.1	92.9±0.4
Capsule	86.9±0.0	94.6±0.0	94.5±0.6	95.6±0.4	94.6±0.8	97.9±0.4	95.2±0.5	96.5±0.4	96.4±0.3	98.4±0.2	96.2±0.4	96.8±0.6	96.2±0.5	98.5±0.1
Carpet	95.4±0.0	99.3±0.0	97.8±0.2	98.4±0.1	99.4±0.0	99.4±0.1	98.2±0.0	98.5±0.1	99.3±0.0	99.5±0.0	98.4±0.0	98.6±0.1	99.3±0.0	99.5±0.0
Grid	82.2±0.0	98.9±0.0	70.2±2.8	58.8±4.9	96.8±1.0	98.8±0.2	70.8±2.0	62.6±3.2	97.7±0.8	98.9±0.4	77.0±1.8	69.4±1.3	98.0±0.2	99.2±0.1
Hazelnut	94.3±0.0	96.7±0.0	95.4±0.7	95.8±0.6	98.5±0.2	98.2±0.1	96.8±0.3	96.3±0.6	98.7±0.1	98.2±0.1	97.2±0.2	97.6±0.1	98.8±0.0	98.7±0.1
Leather	96.7±0.0	99.2±0.0	98.5±0.1	98.8±0.2	99.3±0.0	99.3±0.0	98.7±0.1	99.0±0.1	99.3±0.0	99.3±0.0	98.8±0.0	99.1±0.0	99.3±0.0	99.4±0.0
Metal nut	61.0±0.0	74.2±0.0	74.6±1.1	89.3±1.4	90.0±0.6	86.2±1.2	80.3±2.1	94.6±1.4	91.4±0.4	89.7±0.9	82.7±3.9	95.9±1.8	92.9±0.4	91.3±0.8
Pill	80.0±0.0	83.0±0.0	84.8±1.0	93.1±1.1	96.4±0.3	95.5±0.2	87.3±0.7	94.2±0.3	97.0±0.2	95.6±0.2	88.9±0.5	94.8±0.4	97.1±0.0	95.8±0.2
Screw	89.6±0.0	97.2±0.0	83.3±0.7	89.6±0.5	94.5±0.4	95.6±0.4	89.8±0.8	90.0±0.7	95.2±0.3	95.6±0.6	90.8±0.2	91.3±1.0	96.0±0.5	96.3±0.5
Tile	77.6±0.0	96.2±0.0	84.1±1.1	94.1±0.5	96.3±0.2	97.7±0.1	87.7±0.2	94.4±0.2	96.5±0.1	97.8±0.1	88.9±0.3	94.6±0.1	96.6±0.1	97.8±0.1
Toothbrush	86.9±0.0	93.2±0.0	97.3±0.3	97.3±0.4	97.8±0.1	99.1±0.1	97.7±0.3	97.5±0.2	98.1±0.1	99.2±0.1	98.4±0.2	98.4±0.4	98.4±0.5	99.2±0.1
Transistor	74.7±0.0	69.2±0.0	90.2±2.8	84.9±2.7	85.0±1.8	87.3±2.6	92.3±2.1	89.6±0.9	88.3±1.0	88.6±0.8	94.0±2.7	90.7±1.4	88.5±1.2	90.3±0.6
Wood	93.4±0.0	96.0±0.0	90.7±0.4	92.7±0.9	94.6±1.0	95.7±1.2	91.9±0.1	93.2±0.7	95.3±0.4	96.4±0.3	92.2±0.1	93.5±0.3	95.4±0.2	96.4±0.4
Zipper	91.6±0.0	98.2±0.0	93.9±0.8	97.4±0.4	93.9±0.8	98.4±0.3	95.4±0.3	98.0±0.1	94.1±0.7	98.3±0.1	96.1±0.2	98.1±0.1	94.2±0.4	98.5±0.1
Mean	85.1±0.0	**90.9±0.0**	89.3±0.9	92.0±1.0	95.2±0.5	**95.8±0.1**	91.3±0.7	93.3±0.6	96.0±0.3	**96.3±0.1**	92.6±0.7	94.3±0.5	96.2±0.3	**96.8±0.1**

Table 20: AUPRO (%) results on MVTec-AD segmentation.

Category	k=0		k=1				k=2				k=4			
	WinCLIP	CLIPFUSION	PaDiM	PatchCore	WinCLIP	CLIPFUSION	PaDiM	PatchCore	WinCLIP	CLIPFUSION	PaDiM	PatchCore	WinCLIP	CLIPFUSION
Bottle	76.4±0.0	88.4±0.0	89.8±0.8	93.5±0.3	91.2±0.4	93.7±0.4	91.7±0.2	93.9±0.3	91.8±0.3	94.1±0.1	92.2±0.2	94.0±0.2	91.6±0.2	94.5±0.3
Cable	42.9±0.0	71.5±0.0	59.1±3.2	84.7±1.0	72.5±2.3	79.7±0.8	66.5±2.8	88.5±0.9	74.7±2.3	82.0±1.0	74.2±1.8	91.7±0.6	77.0±1.1	84.4±1.0
Capsule	62.1±0.0	88.5±0.0	80.0±2.0	83.9±0.9	85.6±2.7	92.5±1.1	82.3±2.1	86.6±1.0	90.6±0.6	94.1±0.2	85.7±1.3	87.8±1.9	90.1±1.5	94.7±0.5
Carpet	84.1±0.0	98.2±0.0	92.9±0.3	93.3±0.3	97.4±0.4	98.3±0.1	93.9±0.2	93.7±0.4	97.3±0.3	98.4±0.1	94.4±0.2	93.9±0.4	97.0±0.2	98.5±0.1
Grid	57.0±0.0	95.7±0.0	41.2±4.6	21.7±9.5	90.5±2.7	96.1±1.1	45.1±3.6	23.7±3.8	92.8±2.5	97.1±0.9	55.5±3.4	30.4±4.6	93.6±0.6	96.9±0.7
Hazelnut	81.6±0.0	93.8±0.0	85.7±1.9	88.3±1.3	93.7±0.9	94.3±0.3	89.4±0.9	89.8±1.3	94.2±0.3	94.7±0.5	90.4±0.7	92.0±0.3	94.2±0.3	95.6±0.6
Leather	91.1±0.0	97.7±0.0	95.6±0.2	95.2±1.0	98.6±0.0	97.8±0.1	96.2±0.2	95.9±0.3	98.3±0.4	97.7±0.1	96.3±0.1	96.4±0.1	98.0±0.4	97.6±0.1
Metal nut	31.8±0.0	74.1±0.0	38.1±1.6	66.7±2.9	84.7±1.1	80.1±1.6	48.2±5.0	79.6±4.2	86.7±0.8	85.8±1.6	54.0±8.8	83.8±5.5	89.4±0.1	87.6±1.1
Pill	65.0±0.0	87.6±0.0	78.9±0.6	89.5±1.6	93.5±0.2	93.9±0.3	84.3±0.4	91.6±0.5	94.5±0.2	94.2±0.2	86.6±0.4	92.5±0.4	94.6±0.3	94.5±0.1
Screw	68.5±0.0	89.5±0.0	51.6±1.7	68.1±1.3	82.3±1.1	84.0±0.8	69.5±2.1	69.0±2.1	84.1±0.5	83.6±1.5	72.3±0.8	72.4±3.1	86.3±1.8	85.9±1.1
Tile	51.2±0.0	91.9±0.0	66.7±1.5	82.5±1.1	89.4±0.4	94.5±0.2	71.9±0.5	82.5±0.5	89.6±0.4	94.7±0.2	73.6±0.9	83.0±0.1	89.9±0.3	94.8±0.1
Toothbrush	67.7±0.0	90.6±0.0	82.1±1.5	79.0±2.4	85.3±1.0	91.6±0.9	83.3±2.6	81.0±0.7	84.7±1.4	92.1±0.3	87.1±1.7	85.5±3.0	86.0±3.3	92.7±0.4
Transistor	43.4±0.0	52.5±0.0	70.3±7.0	70.9±4.6	65.0±1.8	68.8±3.0	76.5±5.5	78.8±1.5	68.6±1.1	71.3±0.6	82.2±7.4	79.5±2.8	69.0±1.1	73.1±1.3
Wood	74.1±0.0	93.1±0.0	86.5±0.6	87.1±1.0	91.0±0.6	95.0±0.8	88.0±0.2	86.8±1.4	91.8±0.6	95.3±0.2	88.4±0.2	87.7±0.4	91.7±0.3	95.3±0.4
Zipper	71.7±0.0	94.0±0.0	81.7±2.0	91.2±1.1	86.0±1.7	95.4±0.6	85.6±0.7	92.8±0.4	86.4±1.6	95.7±0.3	87.2±0.8	93.4±0.2	86.9±0.7	96.0±0.3
Mean	64.6±0.0	**87.1±0.0**	73.3±2.0	79.7±2.0	87.1±1.2	**90.4±0.1**	78.2±1.8	82.3±1.3	88.4±0.9	**91.4±0.2**	81.3±1.9	84.3±1.6	89.0±0.8	**92.1±0.2**

Table 21: AUROC (%) results on VisA classification.

Category	k=0		k=1				k=2				k=4			
	WinCLIP	**CLIPFUSION**	**PaDiM**	**PatchCore**	**WinCLIP**	**CLIPFUSION**	**PaDiM**	**PatchCore**	**WinCLIP**	**CLIPFUSION**	**PaDiM**	**PatchCore**	**WinCLIP**	**CLIPFUSION**
Candle	95.4±0.0	94.3±0.0	70.8±4.1	85.1±1.4	93.4±1.4	92.6±0.7	75.8±2.1	85.3±1.5	94.8±1.0	93.4±1.8	77.5±1.6	87.8±0.8	95.1±0.3	94.0±0.9
Capsules	85.0±0.0	80.3±0.0	51.0±7.8	60.0±7.6	85.0±3.1	83.0±1.2	51.7±4.6	57.8±5.4	84.9±0.8	83.1±0.9	52.7±3.4	63.4±5.4	86.8±1.7	83.0±0.8
Cashew	92.1±0.0	81.7±0.0	62.3±9.9	89.5±4.4	94.0±0.4	89.4±1.7	74.6±3.6	93.6±0.6	94.3±0.5	89.3±1.0	77.7±3.2	93.0±1.5	95.2±0.8	90.8±1.4
Chewinggum	96.5±0.0	96.8±0.0	69.9±4.9	97.3±0.3	97.6±0.8	97.4±0.3	82.7±2.1	97.8±0.6	97.3±0.8	97.6±0.3	83.5±3.7	98.3±0.3	97.7±0.3	97.7±0.3
Fryum	80.3±0.0	88.4±0.0	58.3±5.9	75.0±4.8	88.5±1.9	92.2±1.0	69.2±9.0	83.4±2.4	90.5±0.4	93.1±1.2	71.2±5.9	88.6±1.3	90.8±0.5	93.7±0.4
Macaroni1	76.2±0.0	79.3±0.0	62.1±4.6	68.0±3.4	82.9±1.5	86.8±0.7	62.2±5.0	75.6±4.6	83.3±1.9	87.9±1.1	65.9±3.9	82.9±2.7	85.2±0.9	88.9±1.4
Macaroni2	63.7±0.0	61.8±0.0	47.5±5.9	55.6±4.6	70.2±0.9	72.2±2.1	50.8±2.9	57.3±5.6	71.8±2.0	70.8±2.2	55.0±2.9	61.7±1.8	70.9±2.2	72.7±1.8
PCB1	73.6±0.0	83.7±0.0	76.2±1.2	78.9±1.1	75.6±23.0	91.3±1.3	62.4±10.8	71.5±20.0	76.7±5.2	89.7±4.0	82.6±1.5	84.7±6.7	88.3±1.7	89.7±2.8
PCB2	51.2±0.0	61.6±0.0	61.2±2.0	81.5±0.8	62.2±3.9	69.7±5.3	66.8±2.0	84.3±1.7	62.6±3.7	75.9±3.3	73.5±2.4	84.3±1.0	67.5±2.6	76.4±1.4
PCB3	73.4±0.0	67.8±0.0	51.4±12.2	82.7±2.3	74.1±1.1	76.6±4.5	67.3±3.8	84.8±1.2	78.8±1.9	79.2±2.7	65.9±1.9	87.0±1.1	83.3±1.7	78.4±1.2
PCB4	79.6±0.0	76.9±0.0	76.1±3.6	93.9±2.8	85.2±8.9	91.4±1.9	69.3±13.7	94.3±3.2	82.3±9.9	87.8±5.0	85.4±2.0	95.6±1.6	87.6±8.0	94.1±1.6
Pipe fryum	69.7±0.0	81.5±0.0	66.7±2.2	90.7±1.7	97.2±1.1	95.8±1.1	75.3±1.8	93.5±1.3	98.0±0.6	96.6±0.6	82.9±2.2	96.4±0.7	98.5±0.4	97.0±0.2
Mean	78.1±0.0	**79.5±0.0**	62.8±5.4	79.9±2.9	83.8±4.0	**86.5±0.1**	67.4±5.1	81.6±4.0	84.6±2.4	**87.0±0.5**	72.8±2.9	85.3±2.1	87.3±1.8	**88.0±0.2**

Table 22: AUPR (%) results on VisA classification.

Category	k=0		k=1				k=2				k=4			
	WinCLIP	**CLIPFUSION**	**PaDiM**	**PatchCore**	**WinCLIP**	**CLIPFUSION**	**PaDiM**	**PatchCore**	**WinCLIP**	**CLIPFUSION**	**PaDiM**	**PatchCore**	**WinCLIP**	**CLIPFUSION**
Candle	95.8±0.0	94.9±0.0	69.2±3.9	86.6±2.3	93.6±1.5	92.9±0.6	72.8±1.0	86.8±1.7	95.1±1.1	93.9±1.8	72.5±1.1	88.9±1.1	95.3±0.4	94.4±1.0
Capsules	90.9±0.0	88.8±0.0	63.4±5.7	72.3±5.3	89.9±2.5	90.4±0.7	63.4±2.0	73.6±4.7	88.9±0.7	90.6±0.4	63.0±2.3	78.4±3.1	91.5±1.4	90.7±0.3
Cashew	96.4±0.0	91.9±0.0	78.2±5.7	94.6±2.0	97.2±0.2	95.3±0.8	86.1±2.2	96.9±0.3	97.3±0.2	95.2±0.4	88.4±2.0	96.5±0.7	97.7±0.4	95.8±0.6
Chewinggum	98.6±0.0	98.7±0.0	79.8±3.6	98.9±0.1	99.0±0.3	98.9±0.1	89.5±1.9	99.1±0.2	98.9±0.3	99.0±0.1	88.5±3.2	99.3±0.1	99.0±0.1	99.0±0.1
Fryum	90.1±0.0	94.6±0.0	74.5±2.9	87.6±2.4	94.7±1.0	96.6±0.4	81.0±5.4	92.1±1.3	95.8±0.2	96.9±0.5	81.5±3.0	95.0±0.6	96.0±0.3	97.1±0.1
Macaroni1	75.8±0.0	81.1±0.0	60.4±2.9	67.8±3.4	84.9±1.2	88.4±0.9	63.1±4.3	74.9±5.2	84.7±1.5	88.9±0.9	64.9±2.1	82.1±3.5	86.5±0.6	89.8±1.3
Macaroni2	60.3±0.0	59.5±0.0	51.7±5.0	54.9±3.2	68.4±1.8	71.0±2.4	52.7±1.5	57.2±2.6	70.4±1.8	68.3±4.9	54.9±2.5	60.2±3.0	69.6±2.8	70.9±3.3
PCB1	78.4±0.0	87.0±0.0	68.6±2.4	72.1±2.5	76.5±19.0	91.2±1.4	60.4±7.7	72.6±16.4	78.3±4.3	89.2±4.2	77.4±2.9	81.0±9.2	87.7±1.7	89.3±3.5
PCB2	49.2±0.0	66.8±0.0	63.3±1.2	84.4±0.4	64.9±3.3	69.8±5.1	68.9±2.6	86.6±1.1	65.8±4.0	75.7±3.2	75.0±1.7	86.2±1.0	71.3±3.4	75.5±2.0
PCB3	76.5±0.0	70.3±0.0	52.3±10.8	84.6±1.5	73.5±1.6	79.5±3.3	65.2±3.8	86.1±0.5	80.9±1.6	80.9±2.9	64.5±2.4	88.3±1.1	84.8±1.8	81.0±1.4
PCB4	77.7±0.0	78.5±0.0	74.7±2.6	92.8±3.1	78.5±15.5	88.8±3.1	67.6±11.9	93.2±3.4	72.5±16.2	84.8±5.6	84.0±2.0	94.9±1.2	85.6±8.9	91.9±2.1
Pipe fryum	82.3±0.0	90.5±0.0	79.2±1.5	95.4±0.6	98.6±0.5	98.0±0.6	84.5±1.7	96.8±0.7	99.0±0.3	98.4±0.3	89.8±1.7	98.3±0.3	99.2±0.2	98.6±0.1
Mean	81.2±0.0	**83.6±0.0**	68.3±4.0	82.8±2.3	85.1±4.0	**88.4±0.2**	71.6±3.8	84.8±3.2	85.8±2.7	**88.5±0.5**	75.6±2.2	87.5±2.1	88.8±1.8	**89.5±0.1**

Table 23: AUROC (%) results on VisA segmentation.

Category	k=0		k=1				k=2				k=4			
	WinCLIP	**CLIPFUSION**	**PaDiM**	**PatchCore**	**WinCLIP**	**CLIPFUSION**	**PaDiM**	**PatchCore**	**WinCLIP**	**CLIPFUSION**	**PaDiM**	**PatchCore**	**WinCLIP**	**CLIPFUSION**
Candle	88.9±0.0	97.5±0.0	91.7±2.2	97.2±0.2	97.4±0.2	98.4±0.2	94.9±0.8	97.7±0.3	97.7±0.1	98.5±0.1	95.4±0.2	97.9±0.1	97.8±0.2	98.6±0.1
Capsules	81.6±0.0	96.1±0.0	70.9±1.1	93.2±0.9	96.4±0.6	97.8±0.3	75.7±1.7	94.0±0.2	96.8±0.3	97.9±0.5	79.1±0.7	94.8±0.5	97.1±0.2	97.9±0.1
Cashew	84.7±0.0	72.5±0.0	95.5±0.6	98.1±0.1	98.5±0.2	98.2±0.3	96.4±0.4	98.2±0.2	98.5±0.1	98.5±0.1	97.2±0.3	98.3±0.2	98.7±0.0	98.0±0.5
Chewinggum	93.3±0.0	99.1±0.0	90.1±0.4	96.9±0.3	98.6±0.1	99.0±0.1	93.1±0.7	96.6±0.1	98.6±0.1	98.9±0.1	94.4±0.5	96.8±0.1	98.5±0.1	98.8±0.1
Fryum	88.5±0.0	92.5±0.0	93.3±0.6	93.3±0.5	96.4±0.3	95.2±0.3	94.1±0.6	94.0±0.3	97.0±0.2	96.1±0.3	95.0±0.4	94.2±0.2	97.1±0.1	96.5±0.4
Macaroni1	70.9±0.0	98.6±0.0	89.4±0.9	95.2±0.4	96.4±0.6	99.1±0.1	91.7±0.3	96.0±1.3	96.5±0.7	99.2±0.1	93.5±0.5	97.0±0.3	97.0±0.2	99.3±0.1
Macaroni2	59.3±0.0	96.5±0.0	86.4±1.1	89.1±1.6	96.8±0.4	97.4±0.3	90.1±0.8	90.2±1.9	96.8±0.6	97.5±0.1	90.2±0.3	93.9±0.3	97.3±0.3	97.9±0.2
PCB1	61.2±0.0	91.6±0.0	89.9±0.3	96.1±1.5	96.6±0.6	95.5±0.2	90.6±0.6	97.6±0.9	97.0±0.9	96.2±0.2	93.2±1.5	98.1±1.0	98.1±0.9	97.4±0.9
PCB2	71.6±0.0	91.1±0.0	90.9±1.4	95.4±0.2	93.0±0.4	96.1±0.3	93.9±0.9	96.0±0.3	93.9±0.2	96.7±0.1	93.7±1.0	96.6±0.2	94.6±0.4	97.3±0.3
PCB3	85.3±0.0	88.4±0.0	93.9±0.3	96.2±0.3	94.3±0.3	96.2±0.2	95.1±0.5	97.1±0.1	95.1±0.2	96.9±0.2	95.7±0.1	97.4±0.2	95.8±0.1	97.3±0.2
PCB4	94.4±0.0	93.5±0.0	89.6±0.6	95.6±0.6	94.0±0.9	95.8±0.5	90.7±0.9	96.2±0.4	95.6±0.3	96.7±0.2	92.1±0.5	97.0±0.2	96.1±0.3	97.3±0.2
Pipe fryum	75.4±0.0	87.6±0.0	97.2±0.6	98.8±0.2	98.3±0.2	99.4±0.1	98.1±0.4	99.1±0.1	98.5±0.2	99.4±0.1	98.5±0.1	99.1±0.0	98.7±0.1	99.5±0.0
Mean	79.6±0.0	**92.1±0.0**	89.9±0.8	95.4±0.6	96.4±0.4	**97.3±0.1**	92.0±0.7	96.1±0.5	96.8±0.3	**97.7±0.1**	93.2±0.5	96.8±0.3	97.2±0.2	**98.0±0.1**

Table 24: AUPRO (%) results on VisA segmentation.

Category	k=0		k=1				k=2				k=4			
	WinCLIP	**CLIPFUSION**	**PaDiM**	**PatchCore**	**WinCLIP**	**CLIPFUSION**	**PaDiM**	**PatchCore**	**WinCLIP**	**CLIPFUSION**	**PaDiM**	**PatchCore**	**WinCLIP**	**CLIPFUSION**
Candle	83.5±0.0	93.3±0.0	81.5±5.3	92.6±0.4	94.0±0.4	94.5±0.7	87.3±1.2	93.4±0.6	94.2±0.2	94.8±0.3	88.3±0.7	94.1±0.4	94.4±0.2	95.3±0.3
Capsules	35.3±0.0	83.7±0.0	30.6±1.1	66.6±4.5	73.6±3.5	87.7±3.1	38.4±3.7	67.9±2.3	75.9±1.9	88.0±2.6	43.3±2.0	69.0±3.2	77.0±1.4	87.2±0.7
Cashew	76.4±0.0	92.3±0.0	73.4±2.1	90.8±0.2	91.1±0.8	91.7±1.4	78.4±2.7	91.4±1.0	90.4±0.6	90.1±1.2	81.2±2.8	92.1±0.3	91.3±0.9	89.6±1.5
Chewinggum	70.4±0.0	89.1±0.0	58.1±0.6	78.2±1.3	91.0±0.5	85.9±1.2	63.7±2.4	78.0±0.4	90.9±0.7	85.5±1.0	67.2±1.8	79.3±0.8	91.0±0.4	84.5±0.7
Fryum	77.4±0.0	88.3±0.0	71.1±1.6	78.7±2.3	89.1±1.0	83.2±2.1	71.2±0.8	81.4±2.8	89.3±0.2	84.1±1.7	73.2±1.3	81.0±1.2	89.7±0.5	85.3±1.4
Macaroni1	34.3±0.0	87.7±0.0	62.2±4.4	83.4±1.3	84.6±2.3	90.0±0.5	71.8±2.4	86.2±4.6	85.2±1.4	91.2±0.8	76.6±2.1	89.6±0.7	86.8±0.8	91.8±0.7
Macaroni2	21.4±0.0	75.5±0.0	54.9±3.6	66.0±3.0	89.3±2.4	80.3±2.0	65.6±3.4	67.2±6.5	88.6±1.7	79.2±1.5	65.9±1.5	78.3±0.9	90.5±1.3	83.0±1.8
PCB1	26.3±0.0	73.5±0.0	63.9±1.8	79.0±10.7	82.5±6.0	86.3±0.7	68.4±4.1	86.1±1.7	83.8±5.0	86.1±2.9	70.2±3.3	88.1±2.6	87.9±2.1	84.9±2.8
PCB2	37.2±0.0	73.5±0.0	64.4±3.8	80.9±0.5	73.6±1.5	80.5±1.8	72.9±3.4	82.9±1.8	76.2±0.9	82.8±0.9	71.9±2.6	83.7±1.0	78.0±1.3	84.0±1.9
PCB3	56.1±0.0	66.2±0.0	69.0±1.2	78.1±2.0	79.5±2.5	82.7±1.9	74.0±2.3	82.2±1.1	82.3±1.8	83.1±1.6	77.2±0.8	84.4±1.9	84.2±1.0	81.7±3.1
PCB4	80.4±0.0	81.2±0.0	59.1±1.8	77.9±3.1	76.6±4.1	84.5±1.8	62.6±3.6	79.5±4.8	81.7±1.2	86.1±1.2	67.9±2.6	83.5±2.5	84.2±0.7	88.5±1.0
Pipe fryum	82.3±0.0	95.2±0.0	83.9±0.8	93.6±0.5	96.1±0.6	96.6±0.3	86.9±0.9	94.5±0.4	96.2±0.6	97.2±0.2	88.7±1.3	95.0±0.5	96.6±0.2	97.0±0.2
Mean	56.8±0.0	**83.3±0.0**	64.3±2.4	80.5±2.5	85.1±2.1	**87.0±0.3**	70.1±2.6	82.6±2.3	86.2±1.4	**87.3±0.2**	72.6±1.9	84.9±1.4	87.6±0.9	**87.7±0.5**

A.11 Detailed qualitative results

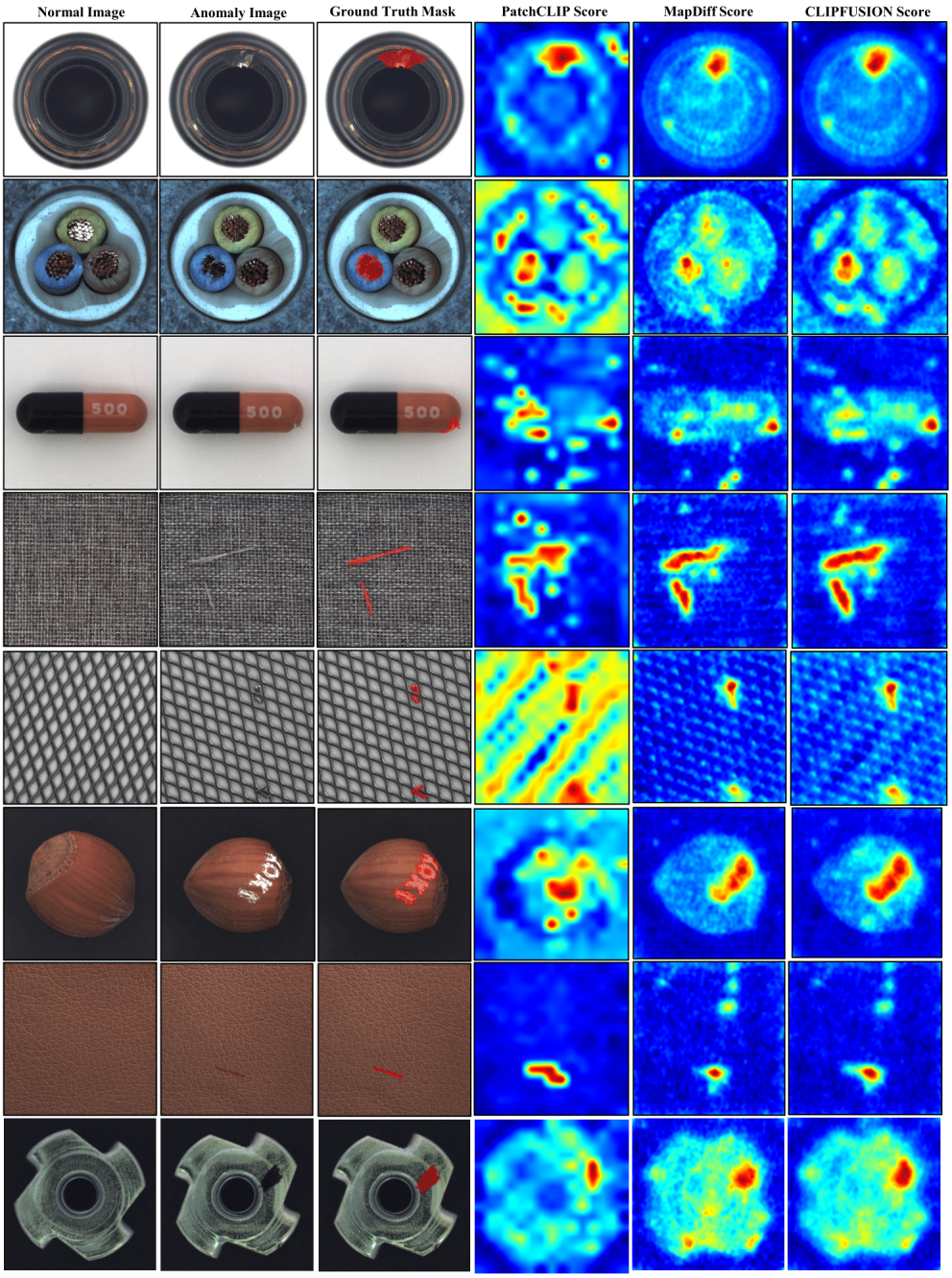

Figure 6: Qualitative results for 0-shot CLIPFUSION with images for PatchCLIP and MapDiff anomaly score maps on MVTec-AD.

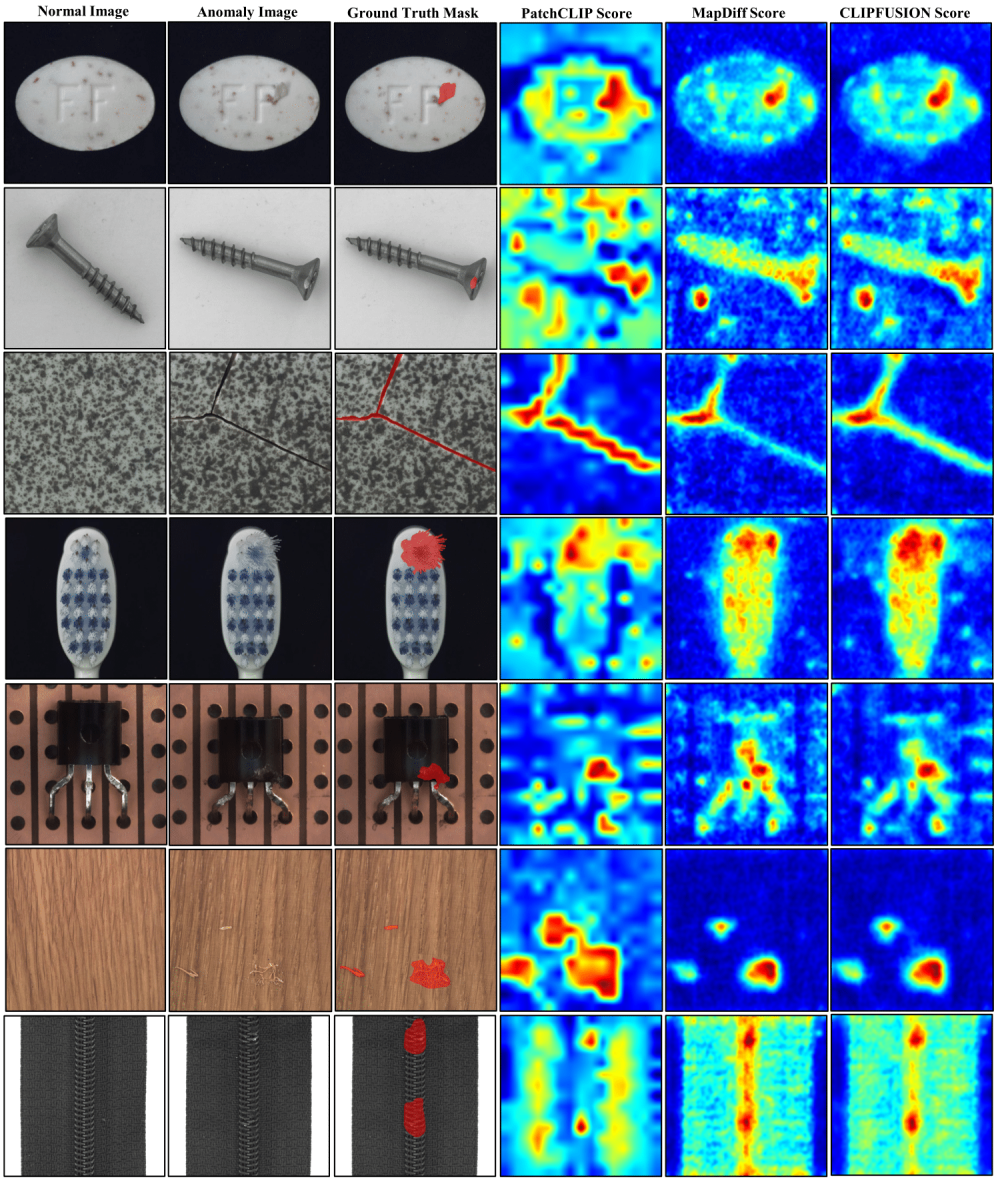

Figure 7: Qualitative results for 0-shot CLIPFUSION with images for PatchCLIP and MapDiff anomaly score maps on MVTec-AD.

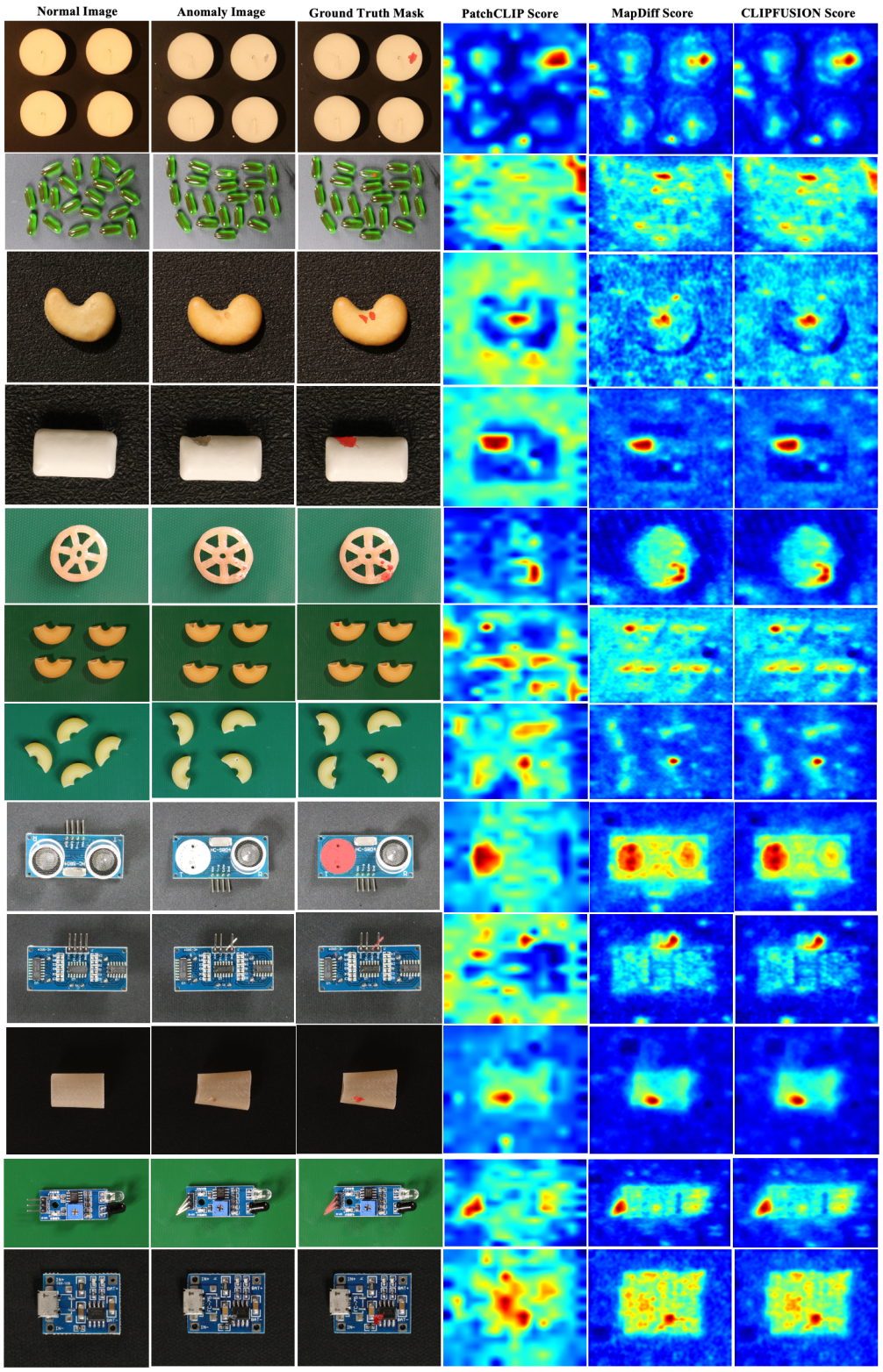

Figure 8: Qualitative results for 0-shot CLIPFUSION with images for PatchCLIP and MapDiff anomaly score maps on VisA.